CHAPTER 4

PEMFC System Modeling and Control

Su Zhou* and **Fengxiang Chen**

Contents

Abstract

Fuel cell system modeling and controller design are the core technologies for better understanding the fuel cell underlying phenomena and safety operations. First, the chapter reviews the fuel cell lumped parameter model, which can represent the mechanism inside of the system. An engineering-oriented PEMFC system lumped parameter model is developed as an example in this chapter. Additionally, an application of Fluent/Simulink collaborative simulation is discussed. A 3D stack model and dynamical models of auxiliary units such as compressor, humidifier, etc.. The controller design of hydrogen purge, heat management, and air supply system in the PEMFC system is

Automotive Engineering College and Clean Energy Automotive Engineering Center, Tongji University, Shanghai, PR China
* Corresponding author, E-mail address: suzhou@tongji.edu.cn

Advances in Chemical Engineering, Volume 41
ISSN 0065-2377, DOI: 10.1016/B978-0-12-386874-9.00007-5

described in details. Moreover, several main control methods such as the conventional PI D control and model predictive control are introduced. Finally, the technologies such as CVM and THDA methods for fuel cell fault diagnosis are introduced.

ABBREVIATIONS

3D	three dimensional
AC	alternating current
ADC	analogue digital converter
CAN	controller area network
CPU	central processing unit
CVM	cell voltage monitoring
DC	direct current
DSP	digital signal processor
FCU	fuel cell control unit
FGR	fast reference governor
GDL	gas diffusion layer
LQR	linear quadratic regulator
LUT	lookup table
MPC	model predictive control
ORR	oxygen reaction reduction
PDEs	partial differential equations
PEMFC	proton exchange membrane fuel cell
PI	proportion integration
PID	proportion integration differentiation
PSO	particle swarm optimization
RAM	random access memory
RG	reference governor
SCM	single-chip microcontroller
SPI	serial peripheral interface
SR	stoichiometry ratio
THD	total harmonic distortion
THDA	total harmonic distortion analysis

1. INTRODUCTION

From the engineering viewpoint, modeling and control are critical for PEMFC system integration and safe operation. As well known, the first-principal model is widely used in chemical processes. However, it is difficult to describe accurately an analytical input/output relationship for a component (subsystem) integrated in a system. Alternatively, a

lookup table or field can be used to set up a complex and nonlinear mapping between the inputs and outputs of the component. Additionally, the transfer function method is applied to model linear or linearized dynamical processes. Such engineering-oriented modeling is sufficient to capture the system dynamics but depends on intensive experimental data. However, an extensive mathematical modeling of multiphysics systems should be combined with advanced numerical techniques could understand fundamentally the interacting electrochemical and transport phenomena. The CFD (computational fluid dynamics) models are commonly used to describe the internal phenomena and guide engineers to optimize fuel cell systems.

The models mentioned above generally fall into two categories: the lumped and distributed parameter models. The lumped parameter models for PEMFC systems are developed based on the mentioned engineering-oriented method. The distributed parameter models are based on the physical conservation laws and coupled partial differential equations (i.e., mass conservation equation, momentum conservation equation, species conservation equation as well as proton/electron conservation). And coupled differential equations are also called CFD model can be used to describe the distribution of important variables such as volume flow rate, species concentration, pressure and temperature, etc. inside a fuel cell or a fuel cell stack. Two phase behaviors can be investigated by the CFD model as well. The combined application of both the lumped and distributed parameter models could be attractive for engineers. Hence, a collaborative simulation method for a PEMFC system is introduced in this chapter. In such simulation, a fuel cell stack is represented by a two-phase CFD model, and auxiliary units such as compressor, humidifier, etc. are modeled by lumped parameter models. Such collaborative simulation can get insight into what may occur within a fuel cell stack by changing the stack boundary conditions resulted from the components models.

The other important aspect for PEMFC systems is to get higher system efficiency or prolong the lifetime. A PEMFC system control is essential to achieve these targets. Generally, the control includes hydrogen supply and purge, air supply, thermal management, and water balance as well as power electronics. Based on author's previous works, hydrogen purge, thermal management, and air supply are selected as control examples in this chapter. In a practical application, the monitoring function is commonly integrated into the control system. In order to avoid critical operating states which can damage a fuel cell stack, the diagnosis is required. Currently, the single-cell voltage or a pair of cells voltage is measured for operating fault diagnosis by cell voltage monitoring (CVM). A fuel cell stacks for automotive application often consists of hundreds

of fuel cells, and the applied CVM is suffering from wiring issues, signal disturbance, etc. Some potentially applicable diagnose techniques, for example, the THDA technique proposed by AVL GmbH, can overcome partily the CVM disadvantages. The THDA method only measures the stack voltage instead of cell voltages.

In this chapter, Section 2 describes the PEMFC system modeling and relative simulations. Section 3 is mainly dealt with the system control and gives also a brief introduction of CVM and THDA methods. The related conclusions are drawn in Section 4.

2. PEMFC SYSTEM MODELING

Computer-based modeling and simulation are essential steps for the PEMFC design, performance evaluation, and optimization. Generally, the published works in this field can be divided into two branches. The first is based on lumped parameter model, (also called dynamical model). Dynamical models are applied not only to fuel cell stack but also to auxiliary units, such as the air compressor, humidifier, hydrogen supply, and cooling system (Zhou, 2004; Zhou *et al*., 2011a). Using the lumped parameter model, the fuel cell output performance, which is influenced by external loads and auxiliary units, can be investigated. The second is based on distributed parameter model developed from simulating a fuel cell to a stack. Using the spatial distribution information of the flow rate, species, temperature, and pressure in a fuel cell (stack), how the electrochemical reaction mechanism, flow field and control strategies, etc. influence the PEMFC system performance can be analyzed (Sun and Zhou, 2009, 2011; Sun *et al*., 2011; Zhou *et al*., 2011b; Zhai *et al*., 2010a,b). This section introduces a lumped parameter model and a collaborative simulation (Mingyan *et al*., 2011; Zhai *et al*., 2010c; Zou *et al*., 2009) for a typical PEMFC system.

2.1 Development of the lumped parameter model

This section proposes a complete mathematical model of a high-pressure PEMFC system which is based on the mechanism and experimental data. The proposed model includes a stack module, an air supplying module, a gas/gas humidifier module, a hydrogen supplying module, and a cooling module, in which some of nonlinear relationships are expressed by lookup tables. This detailed model is implemented into Matlab/Simulink and validated through the experimental data with good agreement. Subsequently, the simulation results based on the proposed model are

presented and analyzed, for example, the profiles of air pressure, temperature, humidity, oxygen stoichiometric ratio, and stack voltage.

2.1.1 The structure of a typical PEMFC system

The schematic diagram of the typical PEMFC system is shown in Figure 1. The PEMFC system includes six main parts. It contains not only the fuel cell stack (the core part of the system) but also the auxiliary units, such as the load, hydrogen/air supply, and cooling/humidifier, which provide the normal working conditions for the stack. The PEMFC system controller starts up the auxiliary units after receiving the load demand. According to the demand, the matched reactant flow rate and pressure are fed by the hydrogen and air supply units, and then the inlet reactant is humidified by the humidifier to balance the water in the stack. The heat management unit adjusts the flow rate and temperature of the coolant to sustain the stack temperature in a safe range.

2.1.2 The model of the PEMFC system

2.1.2.1 Fuel cell stack In order to develop a fuel cell stack model, the following model simplification and assumption are listed:

(1) The distribution of cell voltage in the stack is uniform.
(2) The degree of the relative humidity inside the fuel cell meets the working condition demand of the proton exchange membrane.
(3) The produced liquid water in the stack can be drained timely.

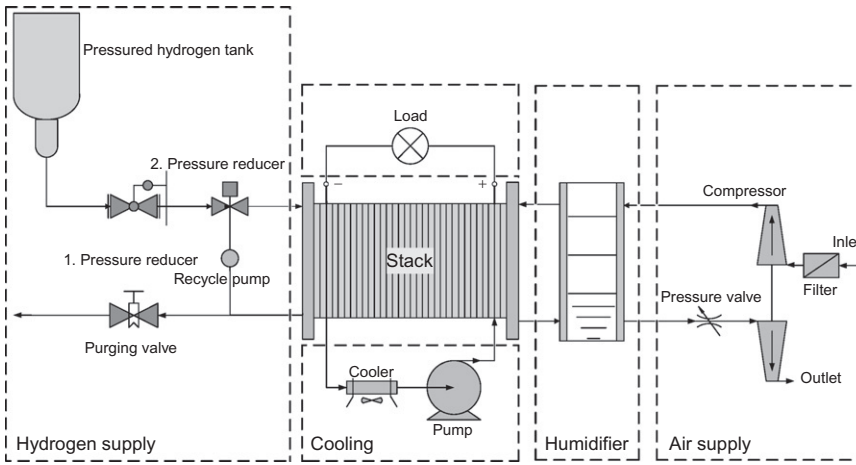

Figure 1 Schematic diagram of a PEMFC system (Zhou *et al.*, 2011a)

The stack model realizes the relation mapping as follows:

$$\begin{bmatrix} I_{st} \\ P_{st} \\ T_{st} \\ \dot{n}_{c,in,air} \end{bmatrix} \rightarrow \begin{bmatrix} U_{st} \\ \dot{n}_{cons,H_2} \\ \dot{n}_{cons,O_2} \\ \dot{n}_{prod,H_2O} \\ \dot{Q}_{st,prod} \\ \lambda_{st,O_2} \end{bmatrix} \tag{1}$$

The relationship between U_{st} and I_{st}, which is one of the ways to show the fuel cell performance, can be expressed by

$$\begin{cases} U_{st} = N_{cell}(E_{cell} - \eta_{act} - \eta_{conc} - \eta_{ohm}) \\ E_{cell} = E_{cell,std} + R_{air}T_{st}\left(\ln\left(P_{H_2}{P_{O_2}}^{1/2}/P_{H_2O}\right)\right)/2F \\ \eta_{act} = \xi_1 \ln(i/i_0) \\ \eta_{conc} = \xi_2 \ln(1 - i/i_0) \\ \eta_{ohm} = iR_{ohm} \end{cases} \tag{2}$$

In Equation (2), there exists the nonlinear relationship between U_{st} and I_{st}, which requires a complex solving process. Hence, Equation (2) is simplified and the following empirical formula is obtained:

$$U_{st} = \lambda_1 + \lambda_2 \ln\left(P_{st,O_2}\right) + (\lambda_3 T_{st} + \lambda_4) I_{st}/A_{cell} \tag{3}$$

where λ_1, λ_2, λ_3, and λ_4 are the parameters to be identified.

The consumed flow rates of hydrogen and oxygen can be computed by Faraday's law:

$$\begin{cases} \dot{n}_{cons,H_2} = N_{cell} I_{st}/2F \\ \dot{n}_{cons,O_2} = N_{cell} I_{st}/4F \end{cases} \tag{4}$$

The oxygen stoichiometric ratio is defined as

$$\lambda_{st,O_2} = \dot{n}_{c,in,O_2}/\dot{n}_{cons,O_2} \tag{5}$$

The generated rate of water and heat can be described by

$$\begin{cases} \dot{n}_{prod,H_2O} = \dot{n}_{prod,H_2} \\ \dot{Q}_{st,prod} = I_{st}\left(E_{st,std} - U_{st}\right) \end{cases} \tag{6}$$

where $E_{st,std}$=$N_{cell}E_{cell,std}$ (according to lower theoretical potential).

2.1.2.2 Air supply The air supply unit involves air compressor, intercooler, gas/gas humidifier, supply channel on the cathode side, back pressure valve, air expander and the connecting pipes, and so on. When the air goes through the above units, the properties of the air (i.e., pressure, temperature, relative humidity, species, and flow rates) will be changed (see Figure 2).

The change of pressure can be obtained by inverse calculating method, given by

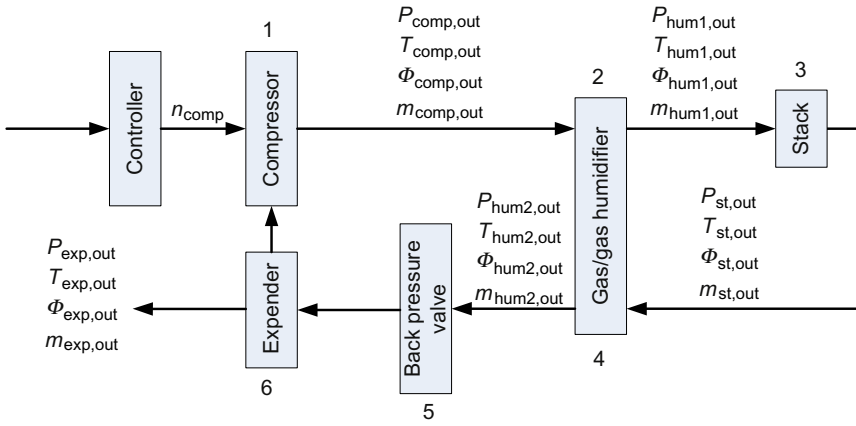

Figure 2 Schematic diagram of an air supply system (Zhou *et al*., 2011a).

$$\begin{cases} P_{i,\text{in}} = P_{i,\text{out}} + \Delta P_i \\ P_{i,\text{out}} = P_{i+\ 1,\text{in}} \\ \Delta P_i = \lambda_{i,\Delta P}\left(3600\dot{n}_{i,\text{out,air}}\left(\bar{T}_i + 273.15\right)R_{\text{air}}/\bar{P}_i\right)^2 \\ P_{6,\text{out}} = P_{\text{amp}} \end{cases} \tag{7}$$

where i represents the components that the air goes through (the order is shown in Figure 2).

$\lambda_{i,\Delta P}$, which is related to the component structure and material property, is the corresponding pressure drop factors. $\bar{T}_i$ and $\bar{P}_i$ are the corresponding average temperature and pressure, defined as

$$\begin{cases} \bar{T}_i = \left(T_{i,\text{in}} + T_{i,\text{out}}\right)/2 \\ \bar{P}_i = \left(P_{i,\text{in}} + P_{i,\text{out}}\right)/2 \end{cases} \tag{8}$$

2.1.2.2.1 Air compressor The air compressor model realizes the mapping as follows:

$$\begin{bmatrix} \text{rpm}_{\text{ref}} \\ P_{\text{amp}} \\ P_{\text{comp,out}} \\ T_{\text{amp}} \end{bmatrix} \rightarrow \begin{bmatrix} \omega_{\text{comp}} \\ PW_{\text{comp}} \\ \eta_{\text{comp}} \\ T_{\text{comp,out}} \\ \dot{n}_{\text{comp,air}} \end{bmatrix} \tag{9}$$

The pressure ratio of the compressor is calculated as

$$K_{\text{pr}} = \frac{P_{\text{comp,out}}}{P_{\text{amp}}} \tag{10}$$

The angular velocity of the compressor is given by

$$\omega_{\text{comp}} = \int_0^t \frac{\text{Tq}_{\text{exp}} + \text{Tq}_{\text{mot}} - \text{Tq}_{\text{fr}} - \text{Tq}_{\text{comp}}}{J_{\text{exp}} + J_{\text{comp}} + J_{\text{mot}}} \text{d}t \tag{11}$$

where

$$\begin{cases} \text{Tq}_{\text{mot}} = \left(K_{\text{p}} + K_{\text{I}}/S\right)\left(\omega_{\text{ref}} - \omega_{\text{comp}}\right) \\ \text{Tq}_{\text{fr}} = K_{\text{fr}}\omega_{\text{comp}} \\ \text{Tq}_{\text{comp}} = \text{PW}_{\text{comp,me}}/\omega_{\text{comp}} \end{cases} \tag{12}$$

$PW_{\text{comp,me}}$ is the compressor shaft power, given by

$$\text{PW}_{\text{comp,me}} = \dot{m}_{\text{comp,air}} R_{\text{air}} \left(T_{\text{comp}} - T_{\text{amp}}\right)\kappa/(1-\kappa) \tag{13}$$

Electric power consumed by the compressor can be given by

$$\text{PW}_{\text{comp,el}} = \text{LUT}_1\left(\text{Tq}_{\text{mot}}, \omega_{\text{comp}}\right) \tag{14}$$

LUT_1 is a lookup table, which is used for calculating the electric power according to the mechanical power.

The compressor efficiency can be calculated by a two-dimensional lookup table as follows:

$$\eta_{\text{comp}} = \text{LUT}_2\left(\text{rpm}_{\text{comp}}, K_{\text{pr}}\right) \tag{15}$$

where $\text{rpm}_{\text{comp}} = 60\omega_{\text{comp}}/2\pi$.

After being compressed by the compressor, the air temperature rise without time lag is

$$T_{\text{comp}} = T_{\text{amp}} + \left[\left(K_{\text{pr}}\right)^{(\kappa-1)/\kappa} - 1\right] T_{\text{amp}}/\eta_{\text{comp}} \tag{16}$$

The corresponding outlet temperature of the air can be estimated by

$$T_{\text{comp,out}} = \text{L}^{-1}\left(\frac{1}{\tau_{\text{comp,temp}}s + 1}\right) * \left(\beta_1 T_{\text{comp}} + \beta_2 T_{\text{amp}}\right) \tag{17}$$

where L^{-1} ( ) is the inverse Laplace transformation, * is the convolution symbol. *Note*: the time lag of the temperature transducer and heat emission factor are considered in Equation (17).

The air-flow rate at compressor outlet is determined by a nonlinear function with independent variables of compressor rotate speed and pressure ratio. In order to develop an accurate compressor model, according to the compressor performance map obtained by experiments, a two-dimensional lookup table is constructed as follows:

$$\dot{m}_{\text{comp,air}} = \frac{P_{\text{std}} T_{\text{amb}}}{(T_{\text{std}} + 273.15) P_{\text{amb}}} \text{LUT}_3\left(\text{rpm}_{\text{comp}}, K_{\text{pr}}\right) \tag{18}$$

Based on the assumption that the air only consists of oxygen, nitrogen, and water vapor, the air molar mass can be calculated approximately by

$$\bar{M}_{\text{air}} \cong \chi_{\text{amp,H}_2\text{O}} M_{\text{H}_2\text{O}} + \left(1 - \chi_{\text{amp,H}_2\text{O}}\right)(0.21 M_{\text{O}_2} + 0.79 M_{\text{N}_2}) \tag{19}$$

where

$$\chi_{\text{amp},H_2O} = R_{\text{air}}\,\text{LUT}_4\left(T_{\text{amp}}\right)/\left(R_{H_2O}P_{\text{amp}}\right) \tag{20}$$

Here, LUT_4 is a lookup table for water saturation pressure calculation. In addition, the molar flow rates of air, oxygen, nitrogen, and water vapor at compressor outlet can be described as follows:

$$\begin{cases} \dot{n}_{\text{comp,out,air}} = \dot{m}_{\text{comp,air}}/\bar{M}_{\text{air}} \\ \dot{n}_{\text{comp,out},O_2} = 0.21\dot{n}_{\text{comp,out,air}} \\ \dot{n}_{\text{comp, out},N_2} = 0.79\dot{n}_{\text{comp,out,air}} \\ \dot{n}_{\text{comp, out},H_2O} = \chi_{\text{amp},H_2O}\dot{n}_{\text{comp,out,air}} \end{cases} \tag{21}$$

2.1.2.2.2 Intercooler The air temperature in compressor outlet is high (>100°C). Therefore, the intercooler has to cool down the outlet air via the cyclic coolant. Assuming

$\dot{m}_{\text{inc,out,air}} = \dot{m}_{\text{comp,out,air}}$ and T_{inc}=$T_{\text{st,in,weg}}$, the heat flow rate is calculated as follows:

$$\dot{Q}_{\text{inc}} = \dot{m}_{\text{inc,out,air}}\text{Cp}_{\text{air}}\left(T_{\text{comp,out}} - T_{\text{inc,out}}\right) \tag{22}$$

2.1.2.2.3 Gas/gas humidifier The gas/gas humidifier model realizes the following mapping:

$$\begin{bmatrix} \dot{n}_{\text{hum1,in},H_2O} \\ \dot{n}_{\text{hum2,in},H_2O} \\ \dot{n}_{\text{hum2,in,air}} \\ \dot{n}_{\text{hum2,in,air}} \\ P_{\text{hum1,out}} \\ P_{\text{hum2,out}} \\ T_{\text{hum1,in}} \\ T_{\text{hum2,in}} \\ T_{\text{inc,out,weg}} \end{bmatrix} \rightarrow \begin{bmatrix} \dot{n}_{\text{hum1,out},H_2O} \\ \dot{n}_{\text{hum2,out},H_2O} \\ j_{\text{hum2,hum1}} \\ P_{\text{hum1,in}} \\ P_{\text{hum2,in}} \\ T_{\text{hum1,out}} \\ T_{\text{hum2,out}} \\ \dot{Q}_{\text{hum1}} \\ \dot{Q}_{\text{hum2}} \end{bmatrix} \tag{23}$$

Here, assuming $T_{\text{hum,out}}$=$T_{\text{hum2,out,weg}}$, $T_{\text{hum2,out}}$=$T_{\text{hum2,out,weg}}$, and the flow rates of oxygen and nitrogen are constant:

$$\begin{cases} \dot{n}_{\text{hum,out},O_2} = \dot{n}_{\text{inc,out},O_2} \\ \dot{n}_{\text{hum,out},N_2} = \dot{n}_{\text{inc,out},N_2} \\ \dot{n}_{\text{hum2,out},O_2} = \dot{n}_{\text{c,out},O_2} \\ \dot{n}_{\text{hum2,out},N_2} = \dot{n}_{\text{c,out},N_2} \end{cases} \tag{24}$$

The water molar flow rate in the membrane humidifier can be calculated by

$$j_{\text{hum1,hum2}} = \frac{D_w A_{\text{mem}}}{L_{\text{mem}}}\left(\frac{\dot{n}_{\text{hum2,in},H_2O}}{V_{\text{hum2}}} - \frac{\dot{n}_{\text{hum1,in},H_2O}}{V_{\text{hum1}}}\right) \tag{25}$$

where D_w is the membrane coefficient of diffusion, which is determined by the following equations:

$$\begin{cases} D_{\mathrm{w}} = \lambda_6 \exp\left(\lambda_5\left(1/303 - 1/T_{\mathrm{inc,out,weg}}\right)\right) \\ \lambda_6 = \begin{cases} 0.1 & \lambda_7 < 2 \\ 0.000001(1 + 2(\lambda_6 - 2)) & 2 \le \lambda_7 \le 3 \\ 0.000001(3 - 1.67(\lambda_7 - 3)) & 3 < \lambda_7 < 4.5 \\ 0.00000125 & \lambda_7 \ge 4.5 \end{cases} \\ \lambda_7 = 0.043 + 8.905\lambda_8 - 9.963{\lambda_8}^2 + 4.5{\lambda_8}^3 \\ \lambda_8 = \dfrac{\dot{n}_{\mathrm{hum1,in,H_2O}} P_{\mathrm{hum1,in}}}{\dot{n}_{\mathrm{hum1,in,air}} \mathrm{LUT}_4\left(T_{\mathrm{hum1,in}}\right)} + \dfrac{\dot{n}_{\mathrm{hum2,in,H_2O}} P_{\mathrm{hum2,in}}}{\dot{n}_{\mathrm{hum2,in,air}} \mathrm{LUT}_4\left(T_{\mathrm{hum2,in}}\right)} \end{cases} \tag{26}$$

The water vapor flow rate in the gas (both dry and wet air) outlet can be calculated by

$$\begin{cases} \dot{n}_{\mathrm{hum1,out,H_2O,g}} = \dot{n}_{\mathrm{hum1,in,H_2O}} + j_{\mathrm{hum1,hum2}} \\ \dot{n}_{\mathrm{hum2,out,H_2O,g}} = \dot{n}_{\mathrm{hum2,in,H_2O}} - j_{\mathrm{hum1,hum2}} \end{cases} \tag{27}$$

The vaporization latent heat is considered in the modeling process. The consumed heat flow rate of the humidifier can be given by

$$\dot{Q}_{\mathrm{hum1}} = rM_{\mathrm{H_2O}}\left(\dot{n}_{\mathrm{hum1,out,H_2O,g}} - \dot{n}_{\mathrm{comp,\,out,H_2O}}\right) \tag{28}$$

It is supposed that there is no dissipate heat through radiation. The heat change in the exhaust air includes two parts, thermal convection with coolant and the phase change of water vapor, and the equations are given by

$$\begin{cases} \dot{Q}_{\mathrm{hum2}} = \dot{Q}_{\mathrm{hum2,conv}} + \dot{Q}_{\mathrm{hum2,late}} \\ \dot{Q}_{\mathrm{hum2,conv}} = \dot{m}_{\mathrm{hum2,out,air}} cp_{\mathrm{air}}\left(T_{\mathrm{hum2,out}} - T_{\mathrm{c,out}}\right) \\ \dot{Q}_{\mathrm{hum2,late}} = \left(\dot{n}_{\mathrm{hum2,out,H_2O,g}} - \dot{n}_{\mathrm{c,out,H_2O,g}}\right) M_{\mathrm{H_2O}} r \end{cases} \tag{29}$$

2.1.2.2.4 Gas pipe The components of the air supply system must be connected by certain pipes. For simplicity, it is assumed that the time lag of the connecting pipes could be added and all of the pipes can be considered as one, which is allocated between the gas inlet of the stack and humidifier. In addition, we suppose the air-flow rate and temperature are constant. There exists a time delay when the air moves through the pipe. This phenomenon can be modeled by

$$P_{\mathrm{ch,out}}(t) = P_{\mathrm{hum1,out}}\left(t - \tau_{\mathrm{ch,pr}}\right) \tag{30}$$

It is assumed the gas temperature in the gas channel outlet of the stack equals to the coolant temperature in the outlet, $T_{\mathrm{c,out}}$=$T_{\mathrm{st,out,weg}}$. The flow rate of nitrogen, oxygen, and water can be calculated by

$$\begin{cases} \dot{n}_{\mathrm{c,out,N_2}} = \dot{n}_{\mathrm{hum1,out}} \\ \dot{n}_{\mathrm{c,out,O_2}} = \dot{n}_{\mathrm{hum,out,O_2}} - \dot{n}_{\mathrm{cons,O_2}} \\ \dot{n}_{\mathrm{c,out,H_2O}} = \dot{n}_{\mathrm{hum,out,H_2O,g}} + \dot{n}_{\mathrm{prod,H_2O}} \end{cases} \tag{31}$$

2.1.2.2.5 Back pressure valve By adjusting the opening of the back pressure valve, the back pressure can be regulated, and then the inlet pressure of the stack is controlled correspondingly. The inlet pressure of the back pressure valve can be calculated by Equation (7), which is influenced by the air mass flow rate. Assuming the back pressure valve operates in its linear range, the air-flow rate through the valve can be written as

$$\dot{m}_{\mathrm{bpv,air}} = K_{\mathrm{bpv}} U_{\mathrm{bpv}} \mathrm{L}^{-1}\left(\frac{1}{\tau_{\mathrm{bpv}} s + 1}\right) \tag{32}$$

where U_{bpv} is the valve control signal.

2.1.2.2.6 Expander The pressure and the temperature of exhausted air at the end of the air supply system are considerably high, which energy can be used. The exhausted air drives the expander and the transfer parts of the energy to the coaxial compressor. The torque delivered from expander to compressor can be calculated by

$$\mathrm{Tq}_{\mathrm{exp}} = \mathrm{rpm}_{\mathrm{exp}} \mathrm{LUT}_5\left(\mathrm{rpm}_{\mathrm{exp}}\right) \mathrm{L}^{-1}\left(\frac{1}{\tau_{\mathrm{exp}} s + 1}\right) \tag{33}$$

where $\mathrm{rpm}_{\mathrm{exp}}$=$\mathrm{Kr}_{\mathrm{exp}}\mathrm{rpm}_{\mathrm{comp}}$, and LUT_5 is a lookup table based on experimental data about the speed and torque of the expander.

The outlet pressure of the expander equals to the ambient pressure, and the inlet pressure of the expander can be described by

$$P_{\mathrm{exp,in}} = P_{\mathrm{amp}} \mathrm{LUT}_6\left(\dot{m}_{\mathrm{exp,in,air}} P_{\mathrm{std}} T_{\mathrm{exp}} / \left(P_{\mathrm{exp,in}} T_{\mathrm{std}}\right)\right) \tag{34}$$

where LUT_6 is a lookup table of relationship between the flow rate and pressure ratio obtained from experimental data.

2.1.2.3 Thermal management system Thermal management system regulates the stack working temperature to its setpoint, takes away the electrochemical reaction heat generated through circulated cooling water. Cooling system uses mixed liquor with 50% ethylene glycol and 50% water as the coolant. Its melting point is $T_{\mathrm{weg,melt}}$ and heat capacity changes with temperature. It is assumed that (1) there is no loss of coolant flow in the cooling loop; (2) considering the heat convection through the stack surface; (3) neglecting the radiation heat loss of all units. To simplify the calculation, the temperature of intercooler and gas/gas humidifier are identical. The system diagram is shown in Figure 3.

The cooling model realizes the following mapping:

$$\begin{bmatrix} T_{\text{set}} \\ \dot{Q}_{\text{inc}} \\ \dot{Q}_{\text{hum1}} \\ \dot{Q}_{\text{hum2}} \\ \dot{Q}_{\text{prod}} \\ T_{\text{amp}} \end{bmatrix} \rightarrow \begin{bmatrix} \dot{m}_{\text{rad,out,weg}} \\ T_{\text{inclout,weg}} \\ T_{\text{st,out,weg}} \\ \dot{Q}_{\text{st,sur}} \end{bmatrix} \tag{35}$$

The coolant flow rate at the intercooler outlet can be calculated by

$$\dot{m}_{\text{rad,out,weg}} = K_{\text{p}}\left(T_{\text{set}} - T_{\text{st,out,weg}}\right) * \text{L}^{-1}\left(\frac{1}{\tau_{\text{pump}}s + 1}\right) \tag{36}$$

The coolant temperature in the outlet of the intercooler is given by

$$T_{\text{inc,out,weg}} = \frac{\left(T_{\text{rad,out,weg}} - T_{\text{weg,melt}}\right)\text{LUT}_7\left(T_{\text{rad,out,weg}}\right)}{\text{LUT}_7\left(T_{\text{inc,out,weg}}\right)} + \frac{\dot{Q}_{\text{incl}} - \dot{Q}_{\text{hum1}} + \dot{Q}_{\text{hum2}}}{\dot{m}_{\text{rad,out,weg}}\,\text{LUT}_7\left(T_{\text{inc,out,weg}}\right)} + T_{\text{weg,melt}} \tag{37}$$

where LUT_7 is a lookup table about coolant heat capacity.

Heat convection through the stack surface can be defined as

$$\dot{Q}_{\text{st,sur}} = A_{\text{st,sur}}\alpha_{\text{st,sur}}\left(T_{\text{st,out,weg}} - T_{\text{amp}}\right) \tag{38}$$

The coolant temperature in the outlet of the stack can be calculated by

$$T_{\text{st,out,weg}} = \frac{m_{\text{st}}\text{Cp}_{\text{st}}T_0 + \dot{Q}_{\text{st,prod}} - \dot{Q}_{\text{st,sur}} + \dot{m}_{\text{rad,out,weg}}T_{\text{inc,out,weg}}\,\text{LUT}_7\left(T_{\text{st,out,weg}}\right)}{m_{\text{st}}Cp_{\text{st}} + \dot{m}_{\text{rad,out,weg}}\,\text{LUT}_7\left(T_{\text{st,out,weg}}\right)} \tag{39}$$

2.1.2.4 Hydrogen supply

2.1.2.4.1 Hydrogen inlet pressure The hydrogen inlet pressure on the anode side should maintain a certain pressure difference with the pressure on the cathode side. It is defined as

$$P_{\text{a,in}} = P_{\text{c,in}} + \Delta P_{\text{c,a}} \tag{40}$$

where $\Delta P_{\text{c,a}}$=0.2∼0.5bar is chosen empirically.

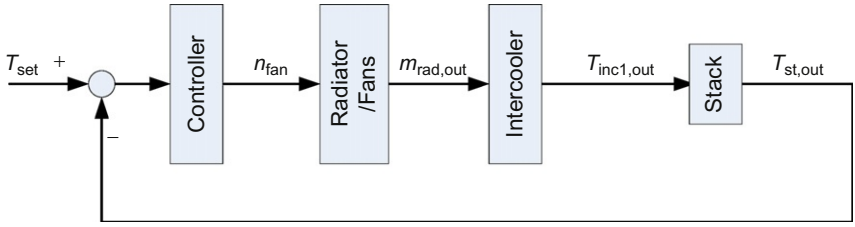

Figure 3 The diagram of the cooling system (Zhou *et al.*, 2011a).

2.1.2.4.2 Hydrogen storage container model Generally, the pressure of vehicle-use hydrogen source is above 350bar, which is far greater than the pressure condition required by the ideal gas equation of state. Hence, actual gas state equation is needed to describe the hydrogen status in the storage container. In practice, the ideal gas equation is usually revised by the pressure ratio factor in the approximate calculation.

Based on the pressure ratio factor, the pressure of the hydrogen storage container can be defined as

$$P_{ve} = z m_{ve,H_2} R_{H_2} T_{ve} / V_{ve} \tag{41}$$

where z=LUT$_8$ (T_{ve}, P_{ve}) the pressure ration factor can be obtained by a two-dimensional lookup table (see Figure 4). m_{ve,H_2} is the hydrogen mass in the container, which can be calculated by

$$m_{ve,H_2} = m_0 - \int_0^t M_{H_2} \dot{n}_{cons,H_2} dt \tag{42}$$

2.1.2.5 Parasitic power The PEMFC system consists of several units, including one compressor, three cycle pumps, and multiple regulating valves. The consumed power by the above units is called parasitic power, which comes from the fuel cell. Due to the parasitic power, the available output power is lower than the total power of fuel cell, that is to say,

$$\mathrm{PW}_{st,gross} = \mathrm{PW}_{st,net} + \mathrm{PW}_{para} \tag{43}$$

where PW_{para} is the parasitic power equal to the sum of the power consumed by the auxiliary units, given by

$$\mathrm{PW}_{para} = \mathrm{PW}_{pump} + \mathrm{PW}_{comp} + \mathrm{PW}_{val} + \mathrm{PW}_{fcu} \tag{44}$$

where PW_{pump}, PW_{comp}, PW_{val}, and PW_{fcu} are the power of cycle pump, compressor, regulating valve, and controller, respectively.

2.1.3 Simulation and results

Based on the developed model above, an implement of a simulation for an 83-kW fuel cell stack in Matlab/Simulink is carried out as an example. The reader can refer to Zhou *et al*. (2011a) for the parameters and calculation details. To simplify the task, we only show the main simulated results in the following.

In order to validate the numerical model presented in the preceding section, comparisons were made to the experimental data. Figure 5 compares the computed polarization curve with the measured one. The simulated curves show a good agreement with the experimental data. Figure 6 shows the demanded current as well as the total current of the stack according to a real load condition. The corresponding output voltage of the stack is shown in Figure 7. In addition, the pressure,

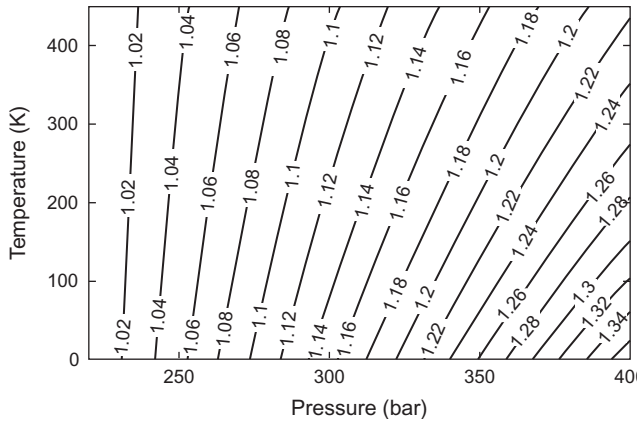

Figure 4 The pressure ration factor of hydrogen (Zhou *et al*., 2011a).

temperature, and relative humidity in different position of the air supply system are shown in Figures 8–10, respectively.

2.2 Fluent/Simulink collaborative simulations

The disadvantages of the two types of fuel cell models can be described as follows: because of the external load changes, which usually take a long time to complete the processes, the distributed parameter models are not suitable for simulations of dynamic working conditions of the stack; the lumped parameter model fails in providing adequate physical understandings for the phenomena occurring inside the fuel cell. The corresponding results are not sufficient to be used for detailed analyses of the fuel cell power systems.

In this section, a collaborative simulation platform for PEMFC systems is presented, where the stack is simulated by a two-phase distributed parameter model and the auxiliary units by lumped parameter models. By exchanging the dynamic data between the external load/auxiliary units and PEMFC stack, dynamic simulation of PEMFC stack has been carried out during the load changes for various states associated with different characteristic variables. The internal states of the stack can be observed while the external load and/or auxiliary units output are changing. Numerical experiments are provided for a special case with multiple cycles of load changes derived from an acceleration mode of a fuel cell vehicle. The numerical results demonstrate that the ''undershoot'' of output voltage is due to the response lag of the auxiliary units and liquid water accumulation in the fuel cell stack.

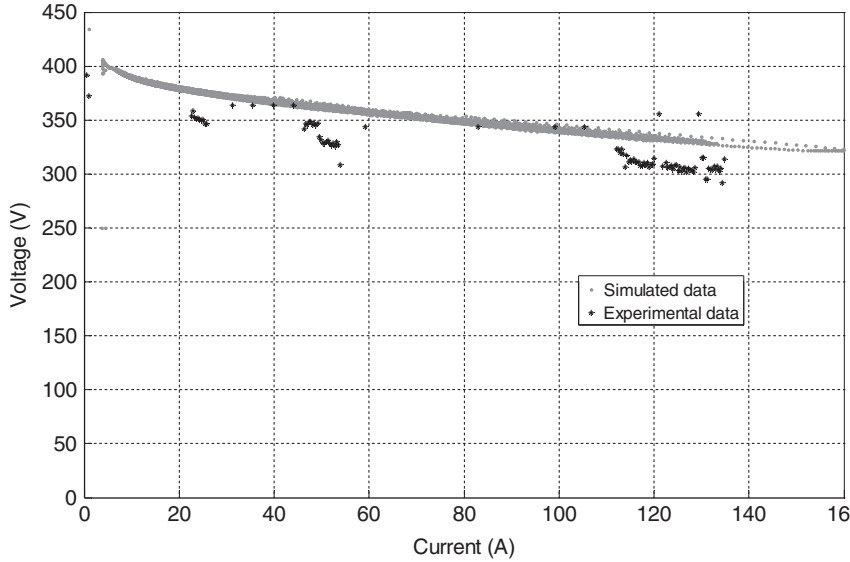

Figure 5 Comparison of predicted and measured stack polarization curve (Zhou *et al.*, 2011a).

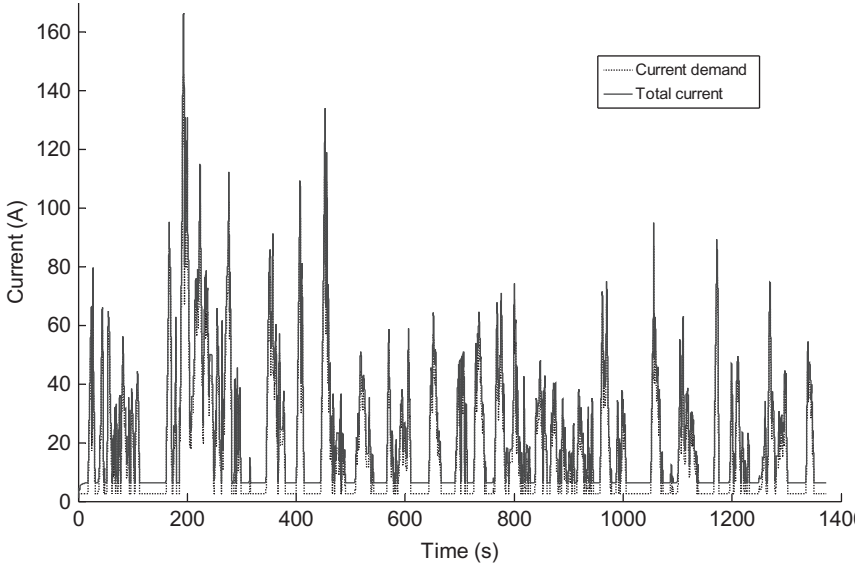

Figure 6 The demanded current and the total current of the stack (Zhou *et al.*, 2011a).

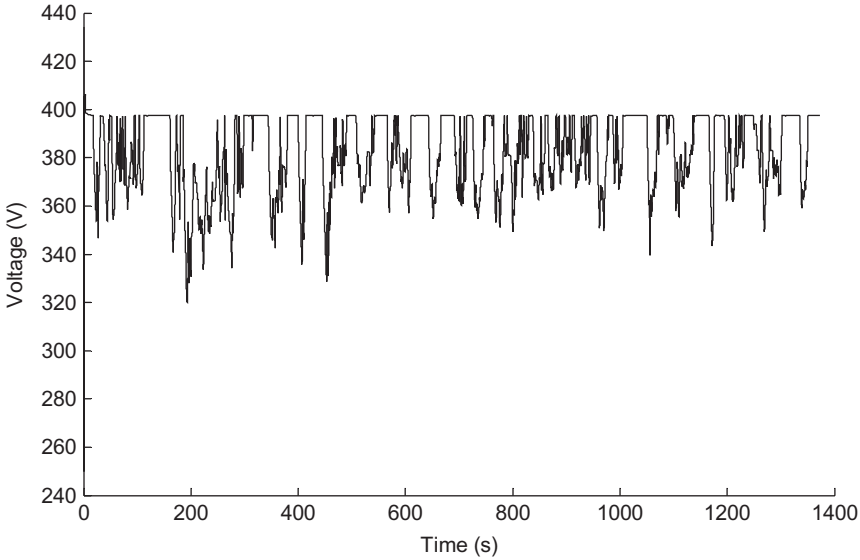

Figure 7 The output voltage of the stack (Zhou *et al*., 2011a).

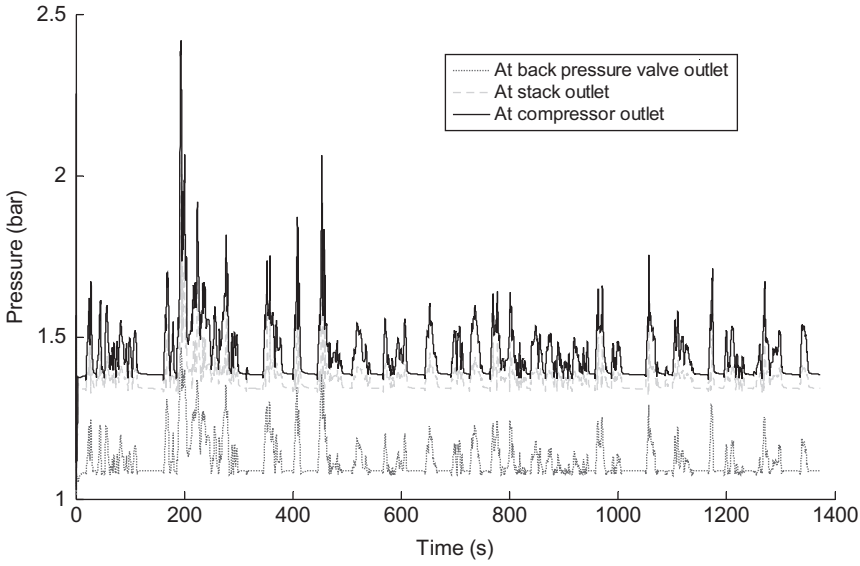

Figure 8 The pressure at different parts of the air supply system (Zhou *et al*., 2011a).

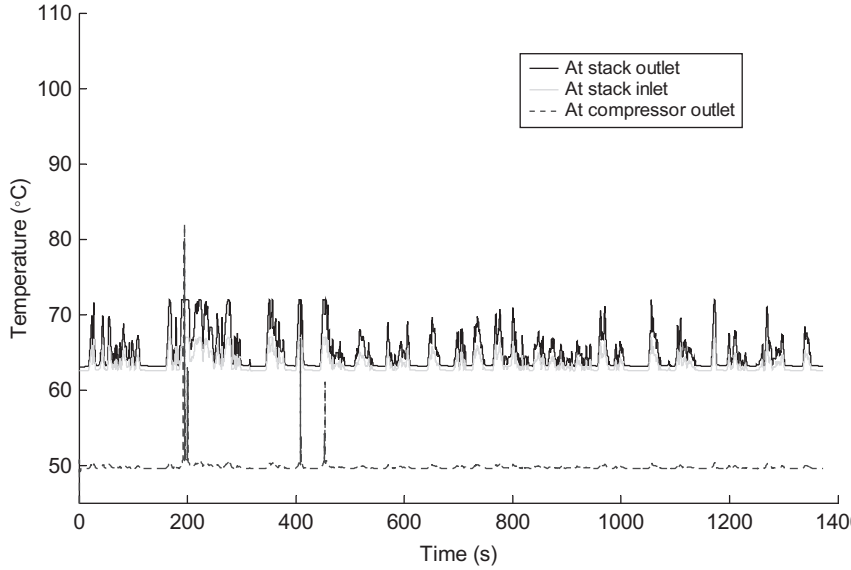

Figure 9 The temperature at different parts of the air supply system (Zhou *et al*., 2011a).

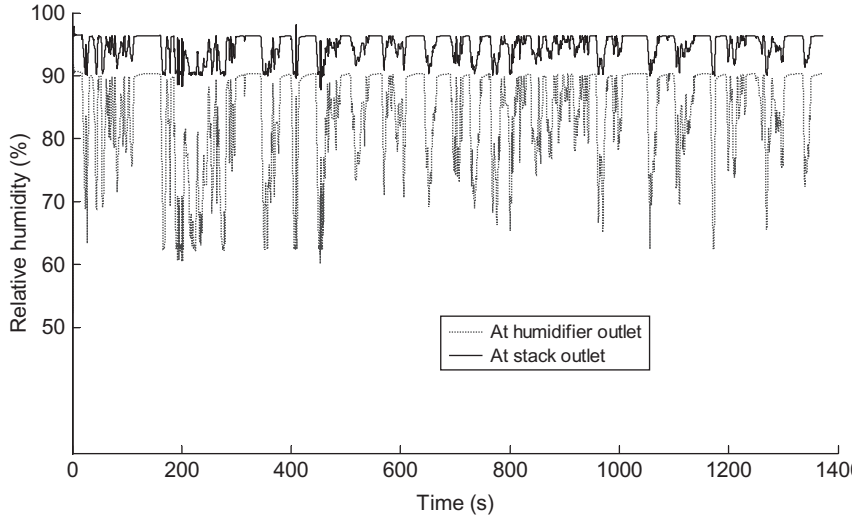

Figure 10 The relative humidity at different parts of the air supply system (Zhou *et al*., 2011a).

2.2.1 The establishment of collaborative simulation platform

A schematic diagram of a typical PEMFC system is shown in Figure 1. Figure 11 illustrates the principle of data transmission in collaborative simulation. Through the inlet boundaries of PEMFC stack, the output signals of the auxiliary units simulated by the dynamic lumped parameter models are passed to the stack and treated as the boundary conditions of the three-dimensional, two-phase transient model of PEMFC stack. Such output signals contain the states of reactant gas and coolant entering the stacks (i.e., flow rate, temperature, pressure, etc.). Based on the boundary conditions transferred from dynamic lumped parameter models, the spatial distributions of physical variables (e.g., temperature, pressure, velocity, species concentration, etc.) are computed by distributed parameter model of the stack, and the numerical results at outlet boundaries are fed back to the corresponding auxiliary units as their input signals. In such way, the collaborative simulation platform for PEMFC system is initially established.

Based on the reasonable model simplifications and assumptions presented previously, we will describe each unit subsequently.

2.2.1.1 Model simplifications and assumptions The main objective is to introduce the model of the stack (3D) and the subsystems and the process of data transfer among them. Hence, the following assumptions were used to develop the model:

(1) The lagging time of humidifier units to meet the requirements for gas humidification is ignored.
(2) Heat transfer effect of the cooling unit is not considered.

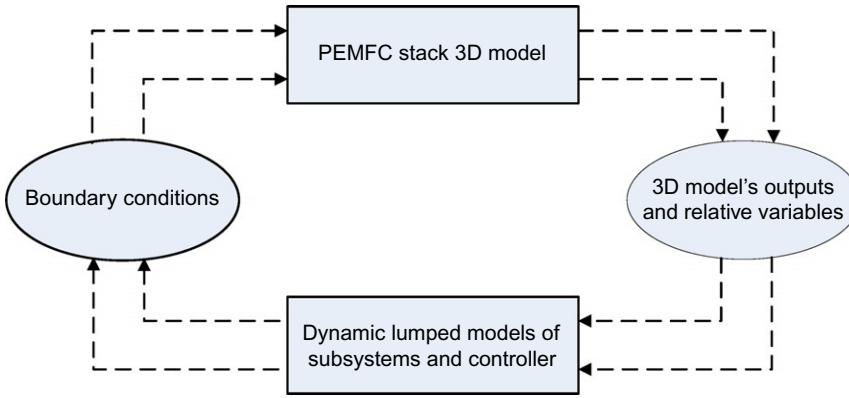

Figure 11 Schematic data transmission of the collaborative simulation (Zhai *et al.*, 2010c).

(3) Both the water vapor and liquid water exist in the stack.
(4) The deformation of fuel cell is not considered.
(5) The effect of the gravity force is not taken into account.
(6) Ideal gas law is employed for the gaseous species.
(7) The porous media including membrane, catalyst layers, and GDL are considered to be isotropic.
(8) The auxiliary units precisely match the simulated PEMFC stack.

2.2.1.2 Hydrogen supply The hydrogen supply mainly consists of pressurized hydrogen tank, pressure reducing valves, hydrogen exhausting valves, and pressure sensor. The hydrogen mass flow rate (kg/s), $\dot{m}_{\mathrm{H_2}}^{\mathrm{in}}$, is based on the target current density, i_{ref}, and stoichiometry, ζ_{a}, defined as

$$\dot{m}_{\mathrm{H_2}}^{\mathrm{in}} = \frac{i_{\mathrm{ref}} A_{\mathrm{mem}} M_{\mathrm{H_2}} \zeta_{\mathrm{a}}}{2F} \tag{45}$$

Besides, according to the cathode inlet pressure change, the operation pressure at anode can be obtained by adjusting the pressure reducing valves to maintain the pressure difference less than 0.2atm.

2.2.1.3 Air compressor The compressor model is separated into two parts. The first part is a static compressor map which determines the air-flow rate through the compressor. The second part represents the compressor and motor inertia and defines the compressor speed. The speed is consequently used in the compressor flow map to find the air mass flow rate, hence, the compressed air mass flow rate $\dot{m}_{\mathrm{Air}}^{\mathrm{in}}$. Air is determined through a compressor flow map which includes the pressure ratio across the compressor and the speed of the compressor, defined as

$$\dot{m}_{\mathrm{air}}^{\mathrm{in}} = \frac{P_{\mathrm{std}} T_{\mathrm{amb}}}{(T_{\mathrm{std}} + 273.15) P_{\mathrm{amb}}} \mathrm{LUT}_1(\mathrm{rpm}_{\mathrm{comp}}, K_{\mathrm{pr}}) \tag{46}$$

where $\mathrm{LUT}_1(\mathrm{rpm}_{\mathrm{comp}}, K_{\mathrm{pr}})$ is a lookup table and $\mathrm{rpm}_{\mathrm{comp}}$ is the compressor speed determined by the current demanded, given as

$$\mathrm{rpm}_{comp} = LUT_2(I) \tag{47}$$

and K_{pr} is the pressure ratio, defined as

$$K_{\mathrm{pr}} = \frac{P_{\mathrm{comp,out}}}{P_{\mathrm{amp}}} \tag{48}$$

where $P_{\mathrm{comp,out}}$ can be retrieved by the feedback value of stack, namely, P_{back} and P_{drop}, respectively. The relationship of them is

$$P_{\mathrm{comp,out}} = P_{\mathrm{back}} + P_{\mathrm{drop}} \tag{49}$$

2.2.1.4 Humidifier Practically, there are many ways to humidify the reactant gases at anode and cathode. However, the crucial factors, which finally determine the humidification effect and the relative humidity, RH, are the gas temperature and the partial pressure of water vapor, defined as

$$\mathrm{RH} = \frac{x_{\mathrm{H_2O}} P}{P_{\mathrm{sat}}(T)} \tag{50}$$

where $x_{\mathrm{H_2O}}$ is the mole fraction of water vapor, P_{sat} is the water vapor saturation pressure, which is a function of temperature only, calculated by

$$\log_{10} P_{\mathrm{sat}} = -2.1794 + 0.02953(T - 273.17) - 9.1837 \times 10^{-5}(T - 273.17)^2 + 1.4454 \times 10^{-7}(T - 273.17)^3 \tag{51}$$

2.2.1.5 Fuel cell stack Fuel cell stack is the core part of PEMFC system, and the goal of the optimization control of all auxiliary units is to sustain the optimal working conditions in order to improve the stack performance and prolong its life. A three-dimensional, non-isothermal, two-phase transient model is developed to describe the transient process of stack. The model consists of a series of nonlinear coupling partial differential equations, representing the conservation of mass, momentum, energy, and charge with electrochemical reaction. The conservation equations are written in the vector form as

$$\partial \varepsilon \rho / \partial t + \nabla \cdot \left(\rho \vec{u}\right) = S_{\mathrm{m}} \tag{52}$$

$$\partial \varepsilon \rho \vec{u} / \partial t + \nabla \cdot \left(\rho \vec{u}\, \vec{u}\right) / \varepsilon^2 = \nabla \cdot (\bar{\bar{\tau}}) - \nabla p + S_{\mathrm{p}} \tag{53}$$

$$\partial (\varepsilon \rho Y_{\mathrm{i}}) / \partial t + \nabla \cdot \left(\rho \vec{u} Y_{\mathrm{i}}\right) = -\nabla \cdot \vec{J_{\mathrm{i}}} + S_{\mathrm{i}} \tag{54}$$

$$\partial (\varepsilon \rho_{\mathrm{f}} E_{\mathrm{f}} + (1 - \varepsilon) \rho_{\mathrm{s}} E_{\mathrm{s}}) / \partial t + \nabla \cdot \left(\rho \vec{u} E\right) = \nabla \cdot \left(k^{\mathrm{eff}} \nabla T\right) + S_{\mathrm{T}} \tag{55}$$

$$\nabla \cdot (\sigma_{\mathrm{mem}} \nabla \phi_{\mathrm{mem}}) + S_{\mathrm{mem}} = 0 \tag{56}$$

$$\nabla \cdot (\sigma_{\mathrm{sol}} \nabla \phi_{\mathrm{sol}}) + S_{\mathrm{sol}} = 0 \tag{57}$$

where $\vec{u}$, p, Y, T, and ϕ denote the intrinsic fluid velocity vector, pressure, mass fraction, and phase potential, respectively. The various source terms, S, of the governing equations and the electrochemical and physical properties are referred to Wang (2004) and Wang and Wang (2005).

Since PEMFC stack is operated under relatively low temperature (<100°C), the water vapor may condense to liquid water, especially at high current densities. To model the formation and transport of liquid water, a saturation model is presented in the channel and defined as

$$\partial (\varepsilon \rho_{\mathrm{l}} s) / \partial t + \nabla \cdot \left(\rho_{\mathrm{l}} \vec{u_{\mathrm{l}}} \nabla s\right) = r_{\mathrm{w}} \tag{58}$$

where s is the volume fraction of liquid water or the water saturation, the subscript l stands for liquid water, and r_{w} is the condensation rate. The convective term is just applied inside the channel. Inside the highly resistant porous zones, the use of the capillary diffusion term allows us to replace the convective term in Equation (14):

$$\partial(\varepsilon\rho_l s)/\partial t + \nabla\cdot\left(\rho_l \frac{Ks^3}{\mu_l}\frac{\mathrm{d}p_c}{\mathrm{d}s}\nabla s\right) = r_w \tag{59}$$

The readers can be properly referred to Zhou *et al*. (2011b) about the definition and the relationship of the above parameters. In addition, $-r_w$ is added to the water vapor equation, as well as the mass source because the condensation is considered.

The above transport equations are then coupled with electrochemical processes through source terms to describe reaction kinetics and electro-osmotic drag in the polymer electrolyte. In addition, a complete form of the electron transport equation shall include a transient term representing the electrochemical double-layer discharging. However, as discussed in Wang and Wang (2005), the time constant of the double-layer discharging ranges from micro- to milliseconds, sufficiently short in order to be safely neglected by automotive fuel cells.

To solve the above system of PDEs, the boundary and initial conditions are required and specified as follows:

Flow inlet boundaries

The velocity is determined by the auxiliary units, and the inlet mass fraction is determined by the inlet pressure and humidity and the relationship:

$$Y_i = x_i M_i / M \tag{60}$$

where M_i is the molecular weight of ith species and M is the average molecular weight. We assume specified value: s=0, T=353.15K, and specified flux: $\partial\phi_{\mathrm{mem}}/\partial n$=0 and $\partial\phi_{\mathrm{sol}}/\partial n$=0.

Outlet boundaries

Fully developed or no-flux conditions are applied:

$$\partial n = 0/\partial n = 0, \partial p/\partial n = 0, \partial Y/\partial n = 0, \partial T/\partial n = 0, \partial\phi_{\mathrm{mem}}/\partial n = 0, \partial\phi_{\mathrm{sol}}/\partial n = 0, \partial s/\partial n = 0 \tag{61}$$

Walls

No-slip and impermeable velocity condition and no-flux condition are applied:

$$\overrightarrow{u} = 0, \partial p/\partial n = 0, \partial Y_i/\partial n = 0, \partial\phi_s/\partial n = 0, \partial s/\partial n = 0 \tag{62}$$

In addition, the boundary conditions for the electronic phase potential, ϕ_{sol}, at the wall terminal on the current collector can be expressed as

$$\begin{cases} \phi_{\mathrm{sol}} = 0, & T = T_0 & \textit{Anode terminal} \\ \partial\phi_{\mathrm{sol}}/\partial n = -I, & T = T_0 & \textit{Cathode terminal} \\ \partial\phi_{\mathrm{sol}}/\partial n = 0, & \partial T/\partial n = 0 & \textit{Otherwise} \end{cases} \tag{63}$$

where I is the current density ($\mathrm{A/m^2}$).

The initial conditions are given by the steady-state field from a previous operation point, except that the inlet boundary conditions are updated by lumped parameter model at each time step. We implement the lumped parameter model for the auxiliary units and the distributed parameter model for the stack by Simulink and Fluent, respectively. The implementation can be elaborated as follows: the real-time data of the auxiliary units are transferred to S-function of the Simulink. Simulink writes the data (i.e., inlet boundary conditions) into the journal file of Fluent, by which the collaborative platform can call Fluent to simulate the stack model. Every time step the data computed by Fluent are saved, and the measurable physical variables at outlet boundaries, such as the back pressure and pressure drop on the cathode, and the hydrogen flow on the anode are fed back to the air compressor and hydrogen supply units, respectively. According to the feedback value, the operating conditions of the next time step (the inlet boundary conditions) are determined by the auxiliary units and transferred to the S-function in order to call Fluent cyclically. Thus, a feedback loop of the collaborative simulation platform is constructed.

2.2.2 Numerical implementation and elucidation

The main objective of this section is to verify the feasibility and effectiveness of the integrated model of PEMFC power systems. Based on the collaborative simulation platform, in this section, we investigate the dynamical response of the stack and auxiliary units to multiple cycles of load change. The description of the stack and its geometric parameters are referred to Zhai *et al*. (2010c).

The simulation takes about 150 h on Dell Inc. OptiPlex 760 (Pentium (R) Dual-Core CPU E5200 @ 2.50 GHz, RAM 3G). Model validation against actual data is needed to verify the reliability of the integrated model of PEMFC power systems. Thus, the simulated results are compared with the experimental data of different references. The reader can refer to Zhai *et al*. (2010c) and Pengtao *et al*. (2008) for the validation in detail.

During the multiple cycles of load change as shown in Figure 12, the dynamic responses of important characteristic variables in the stack, including pressure drop and air-flow rate at cathode, species molar concentration in the catalyst layers, and the water saturation and so on, are stated as follows.

Figure 13 illustrates the pressure drop and air-flow changes in the cathode side with the multiple cycles of load change. We can see that both of the two variables have the similar trend with the smaller current 10 A from t=0 s, 19 s, 52 s to 5 s, 29 s, 60 s, respectively. However, there are big different trend between them under larger current, 60 A and 110 A, from t=7 s, 33 s to 17 s, 48 s, respectively.

According to the lumped parameter model of air compressor, the air-flow rate is determined by the current and the pressure drop plus back pressure as $P_{comp,out}$. Thus, the load increase causes the pressure drop increasing inside the stack, which leads to the air-flow rate increasing too. However, because of the delay of the air compressor, there is no adequate oxygen inside the cathode catalyst layer (see Figure 14). This is the major reason accounting for the ''undershoot'' at t=7.2 and 33.1s. In addition, it is shown that the pressure drop always increases from t=33 to t=48s, but the air-flow rate has little change. The reason is that the major influence factor of the air-flow rate is current under the large load. Furthermore, under the large current, there is more water produced (seen in Figures 14 and 15), which blocks the gas transferring and causes the pressure drop increasing.

Figure 14 displays the dynamic response of species molar concentration at cathode catalyst layers due to load change. It shows the reduction of oxygen molar concentration, but water molar concentration increment change with time. This can be explained in two aspects. First, the lagging time of air compressor leads to the inadequacy of oxygen in the catalyst layers. Second, the liquid water accumulates more and more after the step jump rises in the current, which blocks the oxygen diffusion from the channel to the GDL and catalyst layer, as shown in Figure 15.

Another attractive phenomenon shown in Figure 14 is the nonuniform distribution of species in different parts of the stack. The major reason related to the location and working condition is beyond this paper and further research is needed.

Comparing to the single-phase model, the two-phase model is taken into consideration for the water phase change and is able to capture the phenomena that the pores in the porous medium are obstructed by the liquid water, leading to the blocked reactant transport. Hence, the two-phase model fits the reality better. Figure 15 presents the water saturation profiles on the interface which locates between the cathode diffusion layer

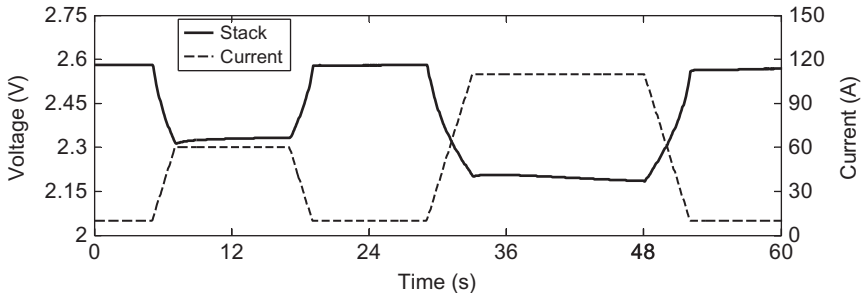

Figure 12 Current and voltage change with time (Zhai *et al*., 2010c).

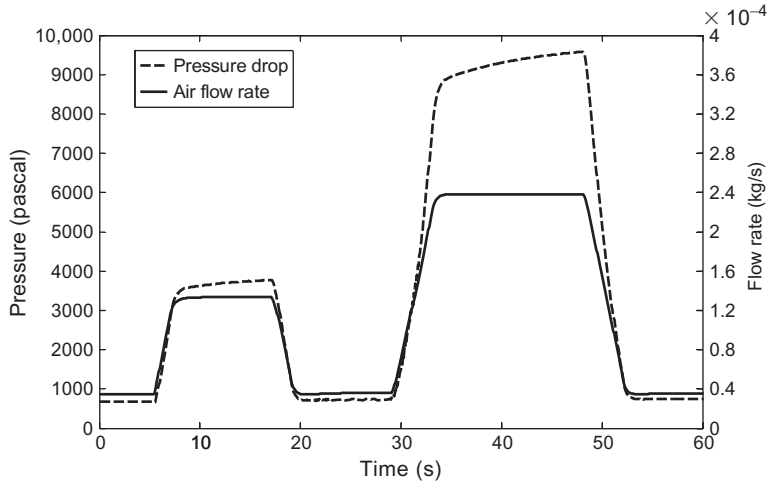

Figure 13 Cathode pressure drop and air-flow change with time (Zhai *et al*., 2010c).

and GDL of cell 2 at various time points. It shows that the water saturation turns out to be larger with time, which indicates that the liquid water accumulation is more severe. This is the major reason why the output voltage decreases from t=33 to 48. The larger water saturation mainly concentrates at the corners and the downstream regions that are close to the outlet of gas channels, especially cathode gas channel. The reason is that the reactant transport is blocked by the accumulating liquid water due to the poor gas purge at the corners, causing more reaction occurs intensively at the location then. The higher water saturation occurring in the downstream is due to the liquid water accumulation from the upstream transport and the stronger local generated water. However, near the cathode outlet the water saturation becomes smaller due to the lower anode RH, which causes more water back diffusion from the cathode to the anode. In addition, due to the ORR (oxygen reaction reduction) near the cathode outlet, the local current is smaller, causing the less generated water.

Thus, the conclusion can be given as: the ''undershoot'' of the output voltage is mainly caused by the auxiliary units' response lag and the liquid water accumulation inside the GDL and catalyst layer. This is a more comprehensive explanation considering both the influences of the auxiliary units and the internal space distribution change inside the stack.

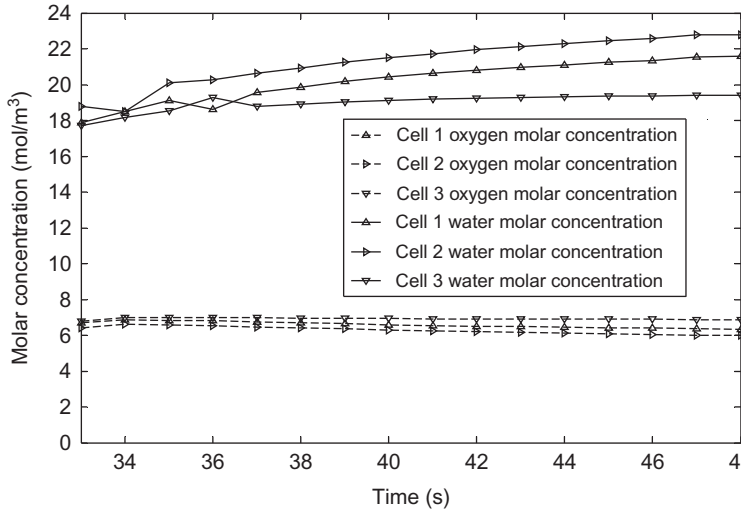

Figure 14 Species molar concentration change with time (Zhai *et al*., 2010c).

2.2.3 Conclusions

The collaborative simulation platform for automobile PEMFC systems is introduced in this chapter, where the stack is simulated by a two-phase distributed parameter model and the auxiliary units by lumped parameter models. Based on the collaborative simulation platform, we can calculate the distributed parameter model of the stack under realizable boundary and initial conditions obtained from the lumped parameter models of auxiliary units. In other words, the proposed collaborative platform can overcome the drawbacks of both lumped parameter model and distributed parameter model. We can utilize the collaborative simulation platform for the following things:

(1) Matching estimate of the auxiliary units and stack.
(2) A useful diagnostic tool. For example, we can investigate the stack based on the polarization curve, current interrupt, pressure drop, and current density mapping (Frano, 2005), which can be all obtained from the collaborative simulation platform.
(3) Investigating in the important characteristic variables (such as the temperature, current, hydrogen, oxygen, and water); Observing the space distribution dynamic response on the auxiliary units change. The collaborative simulation platform could deepen the optimization design of PEMFC power systems for the sake of improving its operational performance from the possible loss due to the auxiliary units change.

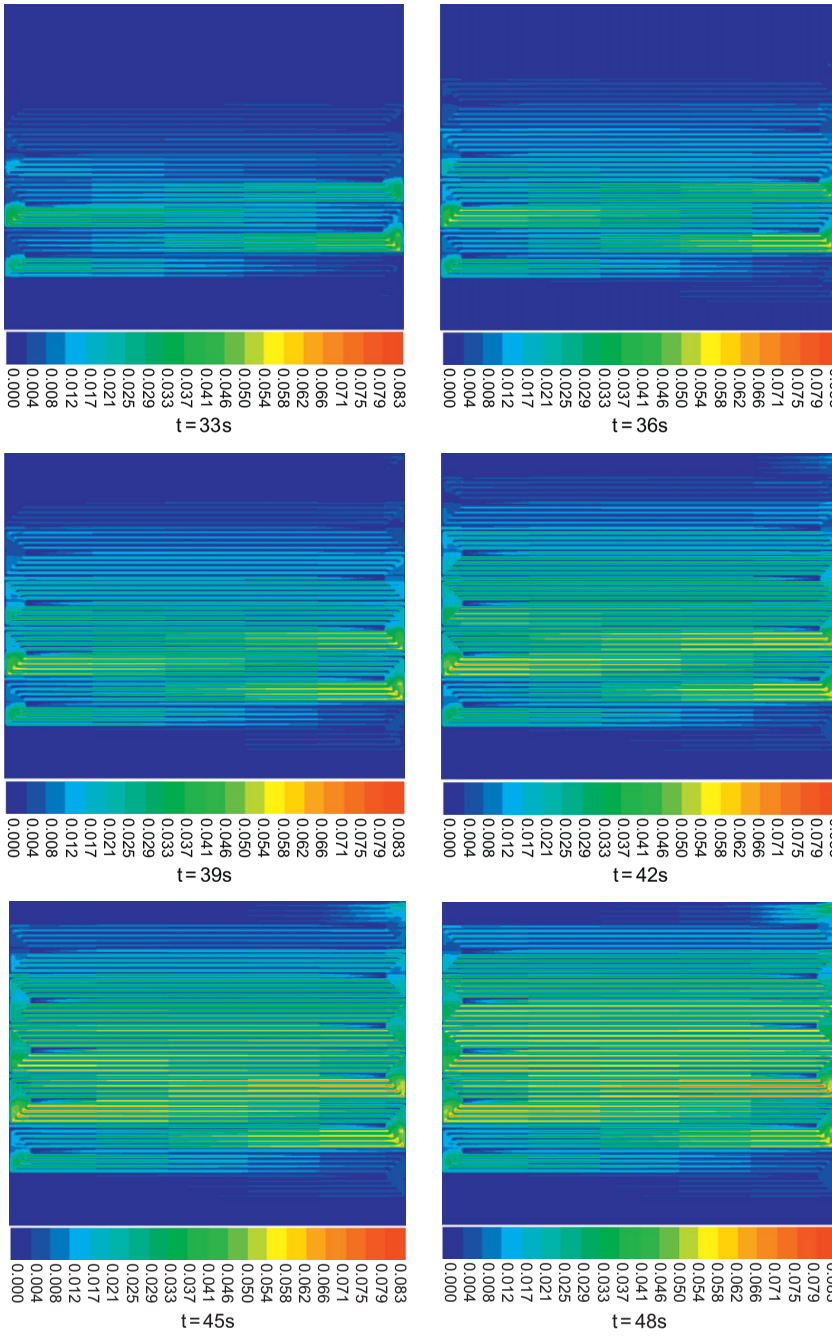

Figure 15 Cathode water saturation change with time (Zhai *et al.*, 2010c).

Thus, we are able to establish a virtual lab which can provide certain significant information for the optimization design of PEMFC power system.

3. CONTROL OF THE PEMFC SYSTEM

Fuel cell power systems have several challenges in control engineering. In the area of PEMFC system for mobile and stationary applications, control plays a critical role in the system integration and safety operations. The objective of a control system is essentially to modify the natural dynamic response of the PEMFC system and maintain the set points in case of uncertainties and disturbances. In addition, the PEMFC system is a typical nonlinear system and has a wide range of operating conditions which could bring a new challenge for the control design.

3.1 Optimal control of the hydrogen purge

3.1.1 Literatures survey

Currently, in order to further enhance the efficiency of PEMFC system and reduce the system complexity, the stack with a dead-ended anode has been used commonly. Thus, an investigation of the hydrogen purge phenomenon, which is in coexistence with the abovementioned model, is clearly of great practical significance.

Himanen *et al*. (2007) reported that anode-side flooding can be reduced at higher hydrogen overpressure due to the increased hydraulic permeation of water through the membrane. Corresponding to hydrogen pressure drops, Corbo *et al*. (2009) showed that a slight voltage recovery due to purge intervention can be observed for those cells that are more affected by the incoming water flooding. Bussayajarn *et al*. (2009) compared the purge effects on different cathode designs (parallel slit, circular open, and oblique slit). They found that the three cathodes' designs are less easy to distinguish as they all reach the same current density level; this is because the cell performance is dominated by water accumulation rather than oxygen transportation. Fabian *et al*. (2006) declared that purge is required to remove the overproduced water, inert impurities presented in the hydrogen, and the nitrogen diffused from the cathode to the anode. The accumulated nitrogen decreases the partial pressure of hydrogen and therefore reduces fuel cell current density. According to their experimental result, Muller *et al*. (2010) also showed that it is necessary to make the purge schedules optimal and safe in order to lessen the water and nitrogen accumulation in the anode. Moreover, Mokmeli and Asghari (2010) studied the effect of impurities in hydrogen on fuel cell voltage and

indicated that if the supply hydrogen with not high purity, no matter dead-end model or flow-through model, the impurities accumulated effect cannot be ignored. Carlson *et al*. (2005) stated that when purge fractions are lower than 0.6%, the increase of the nitrogen concentration in the anode compartment results in a lower cell voltage and hence a lower efficiency. Otherwise, a majority of the freshly fed hydrogen is purged out of the system without being electrochemically utilized, and hence the efficiency is decreased. Furthermore, they also pointed out that a thinner membrane (<50 μm) needs higher hydrogen purge rate in order to avoid anode flooding. Xiao *et al*. (2009) studied two purge patterns, that is, intermittent purge and annular purge, and concluded that the intermittent purge greatly affects fuel cell performance and thus it is not suitable for the *in situ* application; the annular purge process requires a higher pressure drop, and the critical pressure drop is calculated from the annular purge model. The results showed that the annular purge is appropriate for removing liquid water from the anode. Gou *et al*. (2006) also presented a one-dimensional CFD model for PEMFC and found that a long purge time is necessary to show the entire pressure drop curve, while only a part of the curve can be attained if a short purge time is adopted, along with a relatively uniform distribution of pressure swing which represents the top value of pressure variation at certain point in the channel during the purge process. McKay *et al*. (2005) described a simple two-phase flow dynamic model where an anode purge submodel was included as well. This model precisely captured the trend of the voltage recovery after an anode purge event occurs. Based on their model presented in McKay *et al*. (2008), McKay (2008), Siegel *et al*., (2008), and the tunable physical parameters identified by experimental data, McKay *et al*. discussed in detail the relationship between stack performance and anode purge.

3.1.2 Definition of the cost function and selection of the parameters to be optimized

The final element of hydrogen purge control is an electrical valve which is operated periodically. The purge cycle T and purge duration time ΔT can be determined optimally (see Figure 16). As well known, the optimal control typically needs a cost function. In this case, the definition of the cost function should connect the hydrogen utilization ratio and the cell voltage. Such cost function is defined as

$$f_{\mathrm{L}} = \frac{1}{1.25} \frac{\frac{1}{T}\int_0^T u_{\mathrm{stack}} \mathrm{d}t}{1 + 2F\int_0^{\Delta T} \dot{m}_{\mathrm{H_2\_out}} \mathrm{d}t / (M_{\mathrm{H_2}} N_{\mathrm{cell}} I \Delta T)} \tag{64}$$

where f_{L} is the low heat efficiency, u_{stack} is the output voltage, $\dot{m}_{\mathrm{H_{2out}}}$ is the mass flux of exhausted hydrogen, $M_{\mathrm{H_2}}$ is the molar mass of hydrogen,

N_{cell} is the cell numbers, I is the stack current, and F is the faraday constant.

Before optimization, it is necessary to investigate the affects of the purge cycle T and purge duration time ΔT to the cell or the stack performance. In the following sections, the scope of the parameters to be optimized (i.e., the purge cycle T and purge duration time ΔT) can be obtained as the constraints during the optimization.

3.1.2.1 The scope of the parameters It is observed experimentally that the stack voltage will drop gradually if the purge valve is closed due to the accumulation of liquid water inside as well as other impurities (e.g., CO_2, N_2). According to this phenomenon, the maximum time of closing the purge valve (i.e., the upper limit of parameter T) can be determined in case of the allowed lowest stack voltage occurring. Hence, in this case, the upper limit of parameter T is set as 40 s depending on the observation and analysis of the 1-kW stack experimental data. As for the upper limit of the parameter ΔT, it can be chosen a value which is less than the upper limit of the parameter T.

3.1.2.2 Analysis the impaction of parameters to be optimized For studying the interior influence law due to the effect of ΔT on the stack voltage, hydrogen utilization ratio, and stack efficiency, a simulation under 18 A has been carried out. In the simulating process, T=20 s, the value of ΔT is operated from 0.1 to 0.4 s with 0.02 s as the step size. The relevant analysis is given in the following.

First, we should consider the effect of ΔT on stack voltage. In Figure 17, for particular purging cycle under particular current, when purging duration time is too short, the stack voltage will keep dropping, so the stack cannot work normally. As shown in Figure 18, it indicates that the inherent reason of this phenomenon is that the mass of the liquid water in anode channel keeps increasing and leads to flooding inside. In addition,

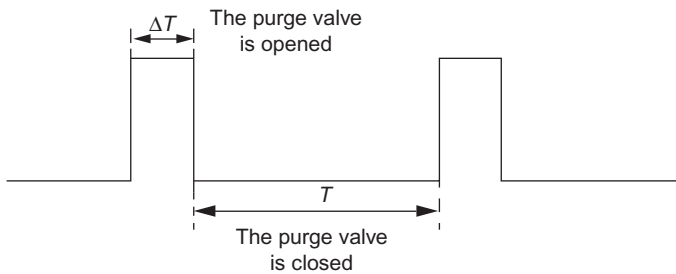

Figure 16 Demonstration of the hydrogen purge.

compare ΔT=0.16s with ΔT=0.40s in Figure 17, it is observed that there are no significant differences on the stack voltage between the both cases.

Then, we analysis the effect of ΔT on hydrogen utilization ratio and stack efficiency. From Figures 19 and 20, we know that for particular purging cycle under specific current, hydrogen utilization ratio and stack efficiency decreased with increasing purge duration time. But, the experiments show that stack cannot keep steady working when ΔT<0.16s, and there is no meaning to study the hydrogen utilization ratio and stack efficiency in such condition. Therefore, the results when ΔT<0.16s are abandoned in Figures 19 and 20.

3.1.2.3 Engineering optimization method In this section, the enumeration method is used to find the optimal value under different specific currents. In order to obtain the corresponding stack efficiency, it is necessary to simulate all discrete points in the scope of parameters and find the maximum. The corresponding point is the optimal value of the parameters. T and ΔT are discredited with the steps as 1 and 0.02s, respectively.

In the enumeration method, first, we can fix $T\in[0,a]$ and find the maximum as $\Delta T\in[d,b]$. Thus, the optimization problem can be rewritten as

$$(T^*, \Delta T^*) = \arg \max_{(T,\Delta T)\in C} f(T, \Delta T) \tag{65}$$

where $C=A\times B$, with $A=[0, a]$, $B=[d, b]$.

Obviously, there are lots of searching methods to solve this problem. For simplicity, here we adopt finite enumeration method, and main conception is mapped out as following: First, the set C is discredited as

$$C_{\mathrm{d}} = \left\{ \left(\frac{ai}{M}, \frac{(b-d)j}{N} \right), \quad i = 0, 1, \ldots, M; \quad j = 0, 1, \ldots N \right\} \tag{66}$$

and thus the original problem can be approximately transformed as

$$(T^*, \Delta T^*) \approx \arg \max_{(T,\Delta T)\in C_{\mathrm{d}}} f(T, \Delta T) \tag{67}$$

Second, since C_{d} is a finite set, the new problem can be easily solved by searching each element of C_{d} and finding out the maximum.

3.1.2.4 The selected results Based on the above optimal method and some typical operate conditions, the simulation results are showed in Figures 21–23. By means of analysis on the results, the optimal values of the two parameters under given operating conditions can be found, and finally, the optimizing of the purge control is achieved.

As shown in Figure 21, under lower current (5A) condition, stack efficiency increases with the increasing cycle time of purge. Hence, in such condition, the optimal purge cycle time can be set as 40s which is the

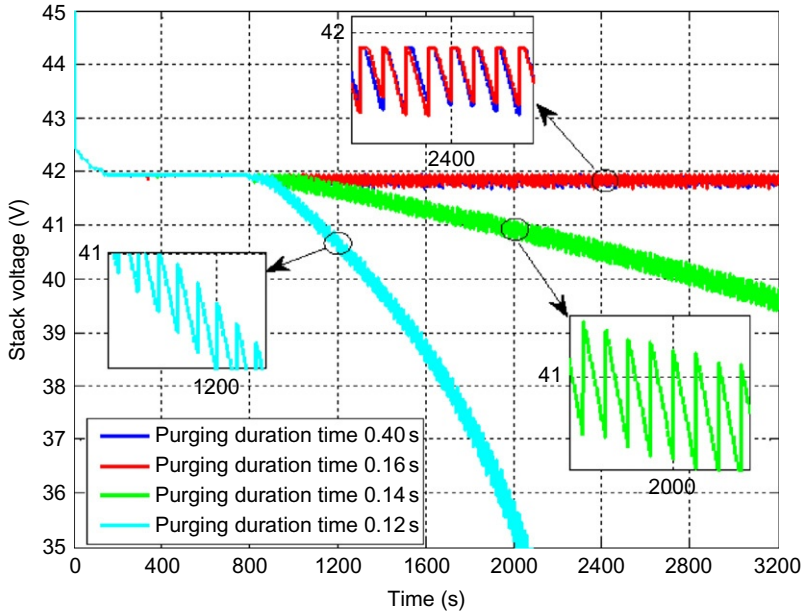

Figure 17 Comparison of the stack voltage under different purge duration times.

upper limit value. Under the medium and high current (14A and 25A) conditions, at first the stack efficiency increases with the increasing cycle time of purge and then keeps unchanged when it reaches a certain level. Therefore, if only the optimized target is considered, the optimum value of purge cycle has a large range. As shown in Figure 22, the value of undulate voltage due to the purge process increases with the increasing cycle time of purge, and the large current boosts this trend.

Once the optimal target is satisfied, there exists the possibility that the life of fuel cell could be taken into account. Under such case, the undulate voltage influence would be ignored. It is obvious that the purge cycle should be as long as possible. Therefore, the optimum parameters regarding to each typical operating condition should be different. As shown in Tables 1 and 2, based on the above analysis and Figure 23, two different optimal results are presented.

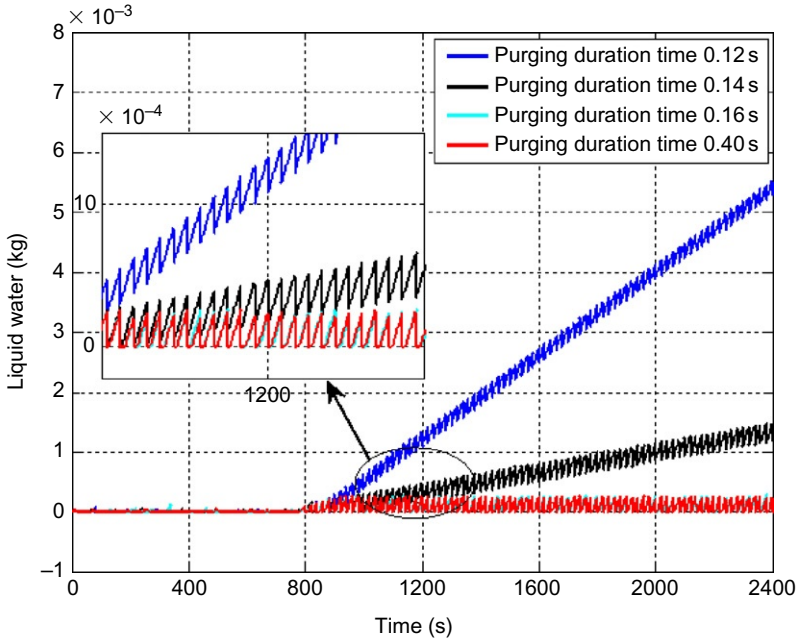

Figure 18 Comparison of the liquid water in channel under different purge duration times.

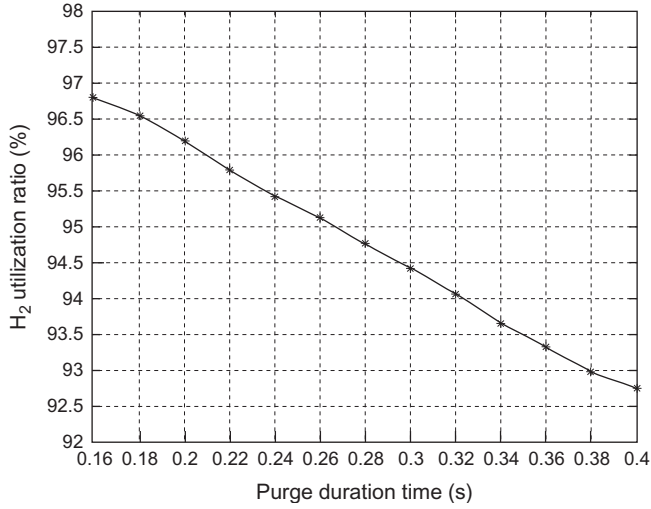

Figure 19 Comparison of the H_2 utilization ratio under different purge duration times.

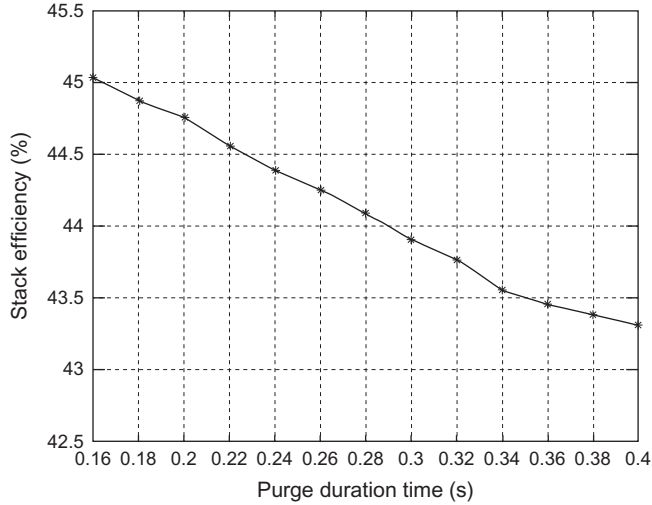

Figure 20 Comparison of the stack efficiency under different purge duration times.

3.2 Heat management for the PEMFC system

3.2.1 Introduction and literature review

A PEMFC produces the similar amount of waste heat to its electric power output; thus, its energy efficiency is about 50%. The thermal energy generated from the PEMFC is mainly made up by electrochemical reaction heat, electric power produced heat, and water phase change heat. The ways of PEMFC thermal transfer include heat conduction, flow heat exchange, convective heat exchange, and radiation heat transfer. Due to operating temperature limit ($<100^{\circ}C$) of PEMFC, radiation heat transfer can be ignored. Forced flow heat exchange and convective heat exchange are the main PEMFC heat transfer methods. The PEMFC performance is directly affected by the PEMFC temperature. A higher operating temperature can result in the cell membrane dehydration and the internal impedance increasing in the fuel cell. Meanwhile, a lower operating temperature may lead to water condensation and flooding at electrodes and, then by added resistance to reactant mass transport, causes a resultant voltage loss. Therefore, in order to make sure the normal operation of the PEMFC, it is necessary to build a heat and water management subsystem to maintain the heat balance of the PEMFC engine system.

Currently, the available control strategies for temperature control are proportion integration differentiation (PID) method, model predictive control (MPC) method, fuzzy control method, etc. Based on the analysis

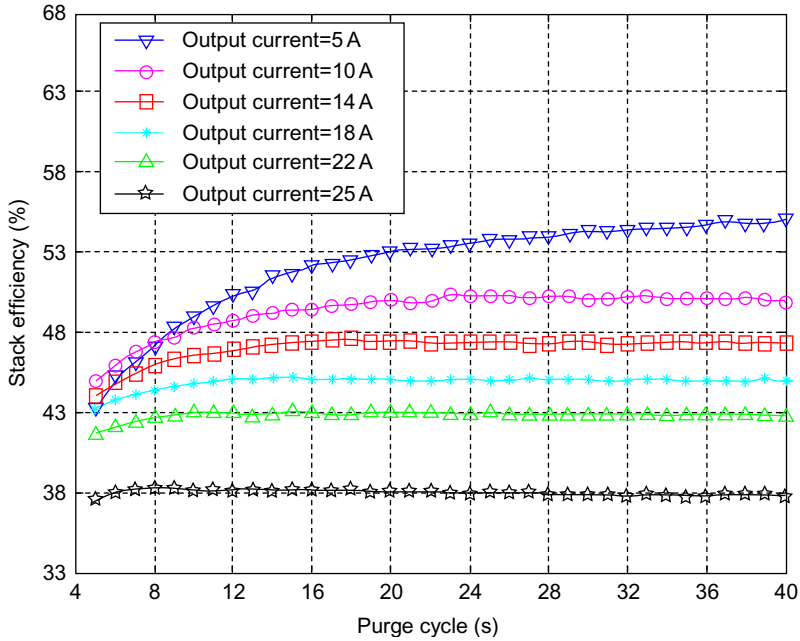

Figure 21 The comparison of stack voltage under different purge cycles.

of PEMFC thermal subsystem, Ouyang *et al*. (Ying and Minggao, 2007; Zhang *et al*., 2004) established the thermal management system model. Due to the big inertia and delay of the thermal system, they designed the intelligent PID control strategy. Because the ordinary PID controller cannot maintain the set point of stack temperature well, for instance, it can hardly eliminate the effect which is generated by the disturbances. The control strategy applied for the thermal system should predict the variation tendency of the PEMFC temperature and take steps to control in advance. Kolodziej established a nonlinear controller to regulate the mass flow of the coolant liquid (Kolodziej, 2007). Li avoided the complex temperature model and adopted the T-S fuzzy model. Based on the T-S fuzzy model, they built the nonlinear predictive controller for controlling the temperature of PEMFC (Li *et al*., 2005). Peng (2010) established the coolant loop model and developed a fuzzy-PID controller for the PEMFC temperature, and the coolant loop model includes fuel cell stack thermal model, radiator model, water tank model, pump model, bypass valve model and so on. Yu (Ahn and Choe, 2008; Shan and Choe, 2005) indicated that the temperature of the fuel cell would change with the load current, the over high temperature of fuel cells will make damage to the

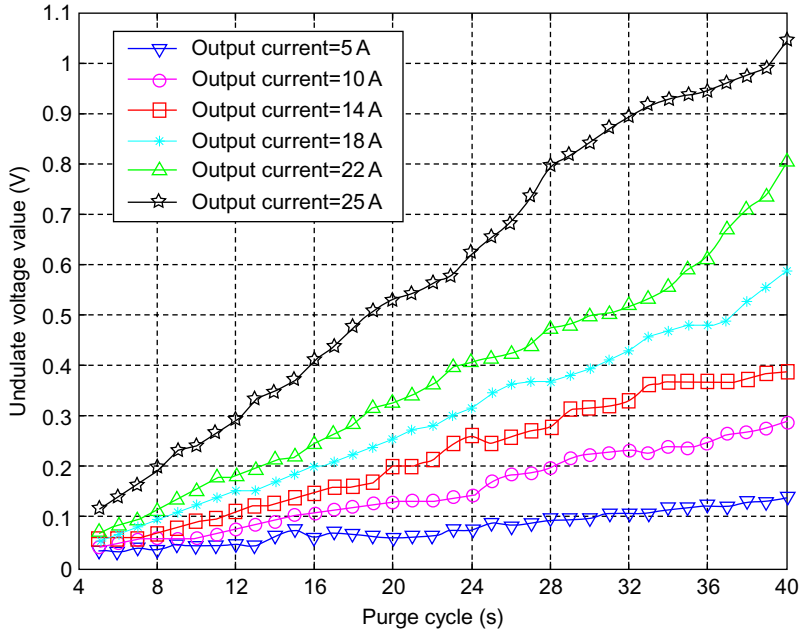

Figure 22 Comparison of the undulate voltage value under different purge cycles.

PEMFC, the coolant loop plays very important role in controlling the temperature of the fuel cell. A PI controller for the coolant loop is employed and had a good control result verified by the experiment data. Cheddie and Munroe (2006) investigated the effect factors about the temperature of the fuel cell. Through comparing several control strategies effects, he pointed that the currently control strategies are limited to control the temperature of the fuel cell well.

3.2.2 Modeling and controller design

As mentioned above, typical PEMFC thermal management system could include coolant tank, cooling pump, intercooler, radiator, radiator fans, coolant pipelines, and so on (see Figure 24). Next there is an example to show the controller design process.

In the PEMFC thermal management system, the main actuator for cooling is the cooling pump. The manipulated variable is the coolant flow $\dot{m}_{\text{coolant}}^{\text{AfterPump}}$. The temperature $T_{\text{coolant}}^{\text{AfterPump}}$ and the pressure $p_{\text{coolant}}^{\text{AfterPump}}$ behind the pump are the system internal states. Additionally, a flow distributor distributes the coolant flows to the fuel cell as well as to the intercooler in the following way:

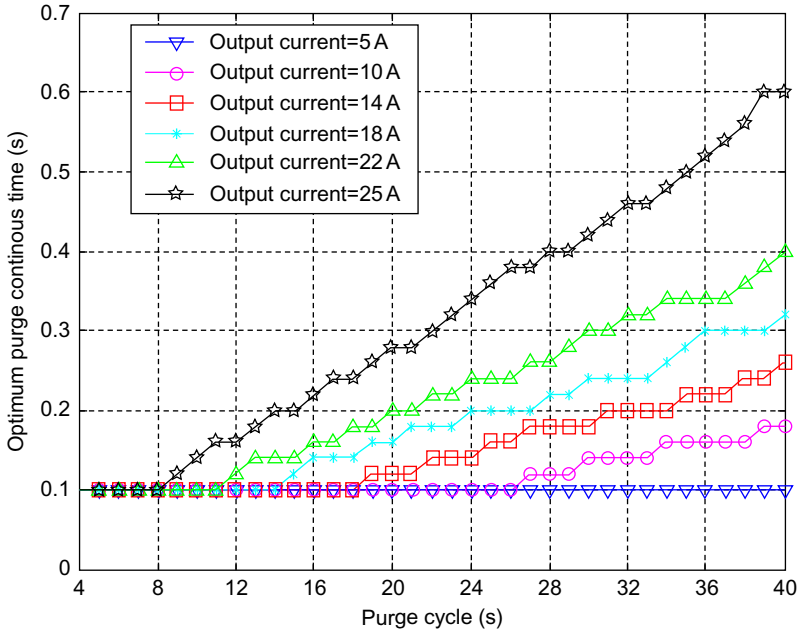

Figure 23 Comparison of the optimum purge continuous time under different purge cycles.

Table 1 The optimum values of purge control parameters under typical operating conditions (consider the effect of undulate voltage)

Output current (A)	5	10	14	18	22	25
Stack efficiency (%)	54.7	50.1	47.3	45.0	42.9	37.8
T (s)	40	24	16	14	12	8
ΔT (s)	0.1	0.1	0.1	0.12	0.12	0.1

Table 2 The optimum values of purge control parameters under typical operating conditions (consider the effect of the life of proton exchange membrane)

Output current (A)	5	10	14	18	22	25
Stack efficiency (%)	54.7	50.1	47.3	45.0	42.9	37.8
T (s)	40	40	40	40	40	40
ΔT (s)	0.1	0.1	0.26	0.32	0.4	0.6

$$\dot{m}_{\text{coolant}}^{\text{ToFC}} = \lambda_{\text{coolant}}\, \dot{m}_{\text{coolant}}^{\text{AfterPump}} \tag{68}$$

$$\dot{m}_{\text{coolant}}^{\text{ToInc}} = (1 - \lambda_{\text{coolant}})\dot{m}_{\text{coolant}}^{\text{AfterPump}} \tag{69}$$

where λ_{coolant} is the flow distributor ratio, $\dot{m}_{\text{coolant}}^{\text{ToFC}}$ is the coolant flow to the fuel cell, and $\dot{m}_{\text{coolant}}^{\text{ToInc}}$ is the coolant flow to the intercooler.

In this cooling process, it can be supposed that the coolant temperature at the stack inlet is equal to the temperature after the pump, and the coolant pressure at the stack inlet is equal to the pressure after the pump, that is, $T_{\text{coolant}}^{\text{ToFC}}=T_{\text{coolant}}^{\text{AfterPump}}$ and $p_{\text{coolant}}^{\text{ToFC}}=p_{\text{coolant}}^{\text{AfterPump}}$. The coolant flow rate remains unchanged when the coolant enters/exists the stack, that is, $\dot{m}_{\text{coolant}}^{\text{OutFC}} = \dot{m}_{\text{coolant}}^{\text{ToFC}}$. The coolant pressure experiences a pressure drop in the stack $\text{dp}_{\text{coolant}}^{\text{Stack}} = \beta_{\text{dpWEG}}^{\text{Stack}}\left(\dot{m}_{\text{coolant}}^{\text{ToFC}}\right)^2$, and the outlet coolant pressure can be calculated as $p_{\text{coolant}}^{\text{OutFC}}=p_{\text{coolant}}^{\text{ToFC}}-\text{dp}_{\text{coolant}}^{\text{Stack}}$.

The heat balance for the stack can be given as follows:

$$m_{\text{Stack}} c_{\text{p}}^{\text{Stack}} \frac{\text{d}T}{\text{d}t} = \dot{m}_{\text{coolant}}^{\text{ToFC}} \int_{T}^{T_{\text{coolant}}^{\text{OutPump}}} c_{\text{p}}(\Gamma)\text{d}\Gamma + \Delta\dot{q}^{\text{Stack}} + (T_{\text{amb}} - T)A_{\text{Stack}}h \tag{70}$$

where $\Delta\dot{q}^{\text{Stack}}$ is the heat produced in the stack. m_{Stack} is the quality of the stack, $c_{\text{p}}^{\text{Stack}}$ is the specific heat capacity of the stack. The solution of above equation is the outlet temperature $T(t)=T_{\text{coolant}}^{\text{OutFC}}(t)$. h is the heat convective coefficient.

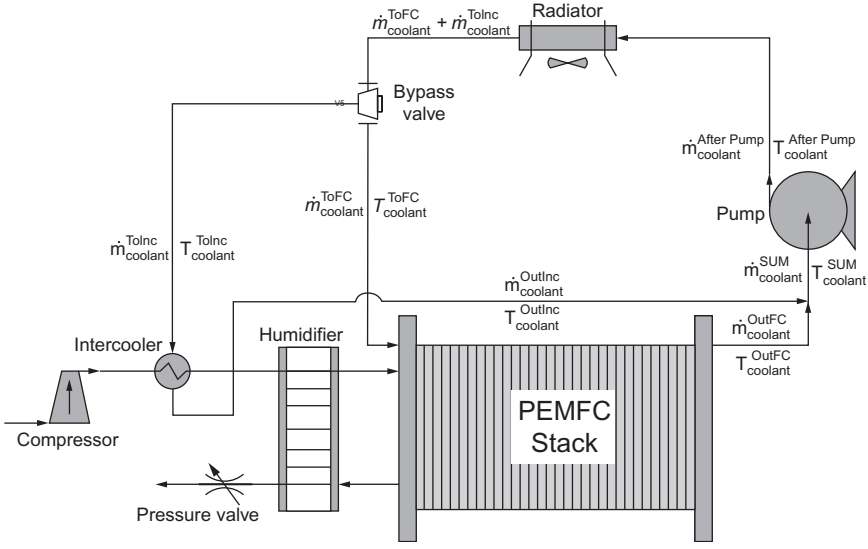

Figure 24 The cooling network diagram for the heat management in a PEMFC system.

The temperature and pressure drop of the coolant in the intercooler are supposed as $T_{\text{coolant}}^{\text{ToInc}}=T_{\text{coolant}}^{\text{AfterPump}}$, $\text{dp}_{\text{coolant}}^{\text{Inc}}=\beta_{\text{dp}_{\text{W}}\text{EG}}^{\text{Inc}}\left(\dot{m}_{\text{coolant}}^{\text{ToFC}}\right)^2$. The coolant flow rate remain unchanged during the cooling process, that is, $\dot{m}_{\text{coolant}}^{\text{OutInc}}=\dot{m}_{\text{coolant}}^{\text{ToInc}}$. The heat balance for intercooler can be given as follows:

$$m_{\text{Inc}}c_{\text{p}}^{\text{Inc}}\frac{\text{d}T}{\text{d}t}=\dot{m}_{\text{E}}^{\text{ToInc}}\int_{T}^{T_{\text{coolant}}^{\text{ToInc}}}c_{\text{p}}(\Gamma)\text{d}\Gamma+\Delta\dot{q}^{\text{Inc}}+(T_{\text{amb}}-T)A_{\text{Inc}}h^{\text{Inc}} \tag{71}$$

where $\Delta\dot{q}^{\text{Inc}}$ is the heat produced in the intercooler, m_{Inc} is the quality of the intercooler, and $c_{\text{p}}^{\text{Inc}}$ is the specific heat capacity of the intercooler. The solution of above equation is the outlet temperature $T(t)=T_{\text{coolant}}^{\text{OutInc}}(t)$. h^{Inc} is the heat convective coefficient.

The coolant flows back to the pump with the mass flow rate $\dot{m}_{\text{coolant}}^{\text{SUM}}=\dot{m}_{\text{coolant}}^{\text{OutInc}}+\dot{m}_{\text{coolant}}^{\text{OutFC}}$, and the temperature of the combined coolant can be calculated as

$$T_{\text{coolant}}^{\text{SUM}}=\frac{T_{\text{coolant}}^{\text{OutInc}}\dot{m}_{\text{coolant}}^{\text{OutInc}}+T_{\text{coolant}}^{\text{OutFC}}\dot{m}_{\text{coolant}}^{\text{OutFC}}}{\dot{m}_{\text{coolant}}^{\text{OutInc}}+\dot{m}_{\text{coolant}}^{\text{OutFC}}} \tag{72}$$

Suppose the coolant pressure $p_{\text{coolant}}^{\text{AfterPump}}$ after the pump is set as constant. The consumed electric power for the pump can be estimated as

$$P_{\text{WEG,el}}^{\text{PUMP}}=10^5\left(p_{\text{coolant}}^{\text{AfterPump}}-p_{\text{coolant}}^{\text{OutFC}}\right)\frac{\dot{m}_{\text{coolant}}^{\text{SUM}}}{\sigma_{\text{WEG}}}\frac{1}{\eta_{\text{WEG}}^{\text{PUMP}}} \tag{73}$$

The maximal heat gradient $\Delta\dot{Q}_{\text{coolant}}^{\text{Max}}/\Delta T$ is depending on the vehicle speed v_{veh} and the coolant mass flow rate $\dot{m}_{\text{coolant}}^{\text{SUM}}$. The relation under standard condition (T_{std},p_{std}) can be mapped into a lookup table $\Delta\dot{Q}_{\text{coolant}}^{\text{Max}}/\Delta T=\text{LUT}_{\dot{\text{Q}}_{\text{max}}}\left(v_{\text{veh}},\dot{m}_{\text{coolant}}^{\text{SUM}}\right)$. Hence, in the ambient (T_{amb}, p_{amb}), the maximal heat taken away can be defined as

$$\Delta\dot{Q}_{\text{max}}=\left(T_{\text{coolant}}^{\text{SUM}}-T_{\text{amb}}\right)\frac{p_{\text{amb}}T_{\text{std}}}{p_{\text{std}}T_{\text{amb}}}\left(\Delta\dot{Q}_{\text{coolant}}^{\text{Max}}/\Delta T\right) \tag{74}$$

Therefore, if the heat required to be removed from the cooling control block is denoted as $\Delta\dot{q}_{\text{req}}$, the corresponding limiting must be carried out $\Delta\dot{q}_{\text{req}}=\min\left(\Delta\dot{q}_{\text{req}},\Delta\dot{Q}_{\text{max}}\right)$. Considering the cooler dynamics, a first-order inertia transfer function is applied as $\Delta\dot{q}_{\text{Is}}=G_{\text{cooler}}(s)\Delta\dot{q}_{\text{req}}$ and $\dot{m}_{\text{coolant}}^{\text{AfterPump}}=G_{\text{pump}}(s)\dot{m}_{\text{coolant}}^{\text{req}}$. As described above, the coolant flow removes the heat produced in fuel cell stack and intercooler.

$$\dot{m}_{\text{coolant}}^{\text{SUM}}\int_{T_{\text{coolant}}^{\text{SUM}}}^{T_{\text{coolant}}^{\text{AfterPump}}}c_{\text{p}}(T)\text{d}T=-\Delta\dot{q}_{\text{Is}} \tag{75}$$

which determines the temperature $T_{\text{coolant}}^{\text{AfterPump}}$ after the pump. The heat $\Delta\dot{q}_{\text{req}}$ required to be removed is calculated in the cooling control block as follows:

$$\Delta\dot{q}_{\mathrm{req}} = \dot{m}^{\mathrm{SUM}}_{\mathrm{coolant}} \int_{T^{\mathrm{FC,dem}}_{\mathrm{coolant}}}^{T^{\mathrm{SUM}}_{\mathrm{coolant}}} c_{\mathrm{p}}(T)\mathrm{d}T \tag{76}$$

where the demanded fuel cell inlet temperature $T^{\mathrm{FC,dem}}_{\mathrm{coolant}}$ is the desired stack operation temperature. Another variable calculated here is the required coolant mass flow rate $\dot{m}^{\mathrm{req}}_{\mathrm{coolant}}$. The heat produced in the stack reaction is the main contribution to the heat to be removed in the whole system; hence, a rough estimation for the required coolant mass flow rate can be carried out as follows:

$$\dot{m}^{\mathrm{req}}_{\mathrm{coolant}} \Delta T_{\mathrm{req}} c_{\mathrm{p}}\left(T^{\mathrm{OutFC}}_{\mathrm{coolant}}\right) = \Delta\dot{q}^{\mathrm{stack}}_{\mathrm{reaction}} = \dot{n}_{\mathrm{H_2}} D_{\mathrm{hr}} - u_{\mathrm{stack}} i_{\mathrm{stack}} \tag{77}$$

where $\dot{n}_{\mathrm{H_2}}$ is the H_2 mole flow rate consumed, D_{hr} the reaction heat of H_2 combustion, and ΔT_{req} the maximal allowed temperature change (max $\{T^{\mathrm{OutFC}}_{\mathrm{coolant}} - T^{\mathrm{ToFC}}_{\mathrm{coolant}}\}$).

The stack temperature controller is designed based on the traditional PID and MPC algorithms. The key parameters for the MPC are given in the following: the system sampling time is 0.1 s; the prediction and control horizons are taken as 10 and 2, respectively.

3.2.3 Simulation and results

Based on the above analysis, a PEMFC thermal management system model is established in the Matlab/Simulink. The PID and MPC control strategies are applied for the controller design. The identical load cycle in Figure 25 is applied during the simulations.

From Figure 26, the compared results between the feedforward+MPC control and the feedforward+PID show that the MPC controller has less response time than PID. When load current changes greatly, the MPC controller gives better performance than the PID (see Figure 27). The MPC strategy can stabilize the temperature to the set point. Due to the nonlinearity and the whole system applies the same PID control parameters, the temperature inevitable deviates the required point under some current condition. So the temperature under PID control will become instability. Moreover, the overshoot of MPC control is smaller than PID.

3.3 Controller design for Air supply system

The PEMFC system can work by continuously feeding the reacting gases (e.g., air). In cathode side of the fuel cell, insufficient oxygen supply can damage the fuel cell stack (Yang *et al.*, 1998), and too much oxygen supply needs more energy to drive the compressor or blower, resulting in lower system efficiency. Hence, it needs a proper control strategy to balance these two conflicting aspects.

3.3.1 Literature surveys

Many contributions regarding air management are collected in this chapter. The current is critical in the air management and commonly treated as a measurable disturbance. However, in some collected contributions, the current is regulated, resulting in another control strategy. Figure 28 shows the aspects of classification, control objectives, control structure as well as controller types in the collected literatures. Based on these aspects, the air management can be divided into two groups: without current regulation and with current regulation.

In the control objective, the air flow rate control is most of interest. There is a variable, namely oxygen stoichiometry ratio (O_2 SR in short), widely used in the air management. It is defined as

$$\lambda_{O_2} = \frac{\dot{m}_{O_2,\text{feed}}}{\dot{m}_{O_2,\text{reacted}}} \tag{78}$$

$\dot{m}_{O_2,\text{feed}}$ (kg/s) represents the oxygen mass flow rate at the stack inlet, and $\dot{m}_{O_2,\text{reacted}}$ (kg/s) represents the oxygen consumption rate by the electrochemical reaction.

Actually, the studies of air supply subsystem control are almost around the control of O_2 SR because it is found experimentally that O_2 SR severely affects the fuel cell system performance. Hence, one of the control objectives can be said to maintain the O_2 SR in an optimal state. Another control objective in air supply subsystem is to maintain a proper pressure in the stack. Indeed, the pressure regulation is coupled with the air-flow rate control. To achieve these objectives, master–slave, feedback+feedforward

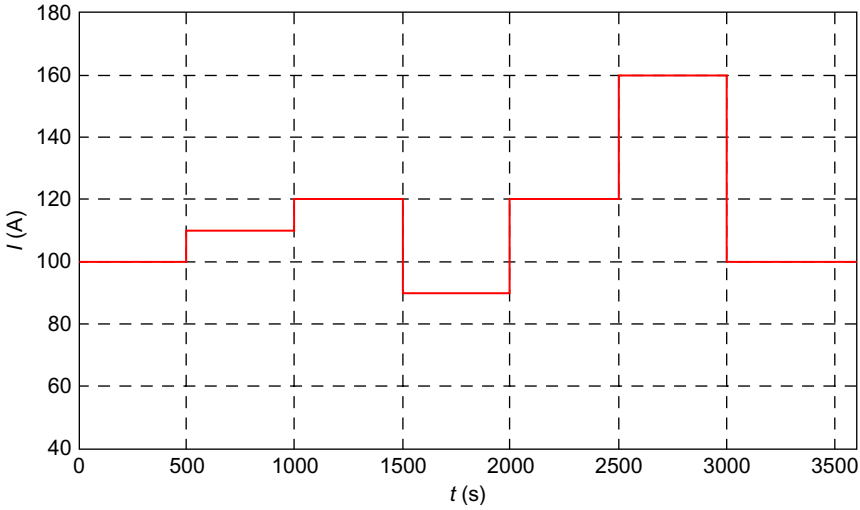

Figure 25 Load cycle of the required current.

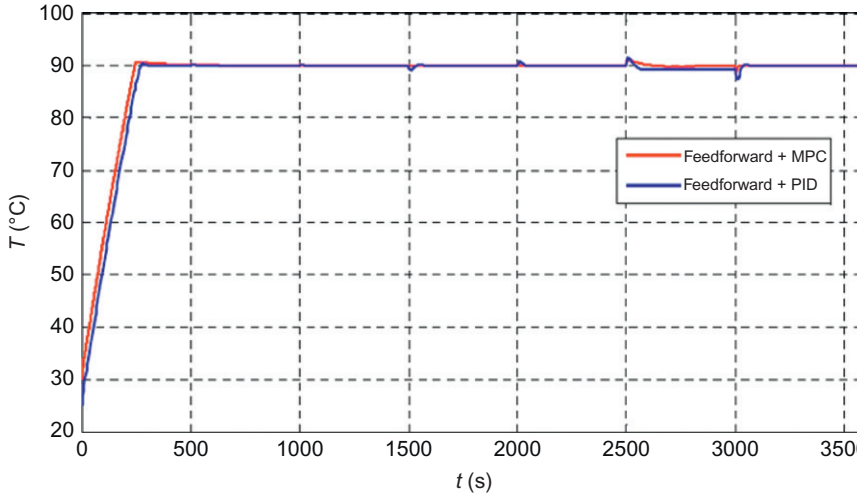

Figure 26 Feedforward+PID and feedforward+MPC.

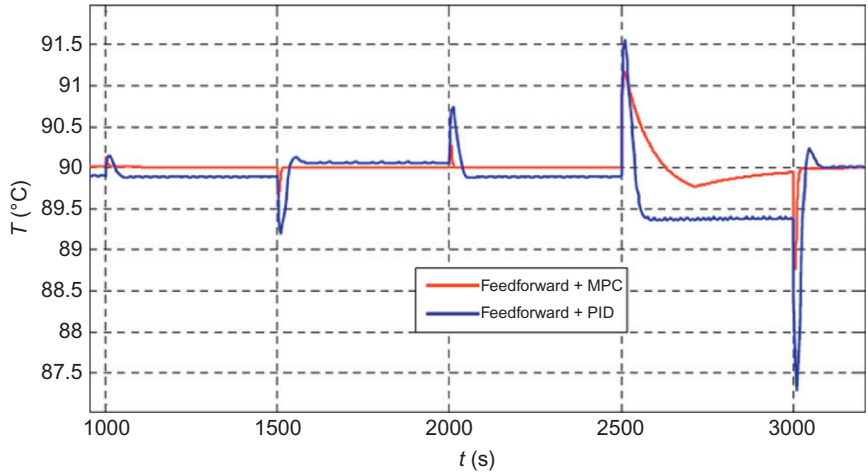

Figure 27 The partial enlarged detail of feedforward+PID and feedforward+MPC.

structure, etc. are widely applied. The controllers in the collected literatures have many types: PID, MPC, fuzzy controller, etc.

3.3.1.1 Air management without current regulation In around 80% collected literatures, the air management without current regulation is discussed. Arce *et al*. (2007) considered three different control strategies: (1) O_2 starvation prevention, (2) maximum system efficiency, and (3) stack

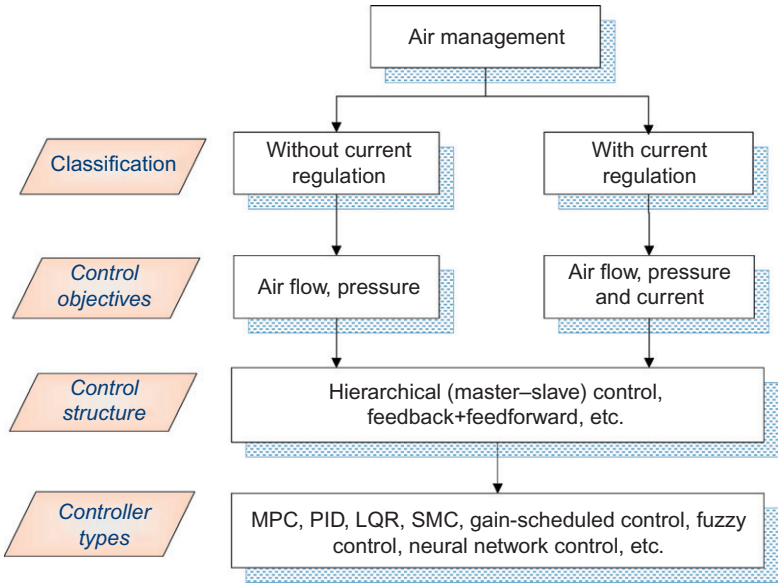

Figure 28 Control strategies for air management.

voltage tracking control. A constrained MPC is applied to achieve two important objects (Arce *et al.*, 2010):

Object #1. The oxygen starvation should be avoided. This can be fulfilled by controlling the O_2 SR bigger than 1.0. During the abrupt load changes, the air flow equipment requires some time to provide the new amount of air to maintain the O_2 SR in safely levels because the electrochemical reaction dynamics are several orders of magnitude higher than gas fluid-dynamics process.

Object #2. High system efficiency or large net power output should be fulfilled by means of an optimal O_2 SR. Based on the relationship between O_2 SR and net power of a PEM fuel cell system under varied current conditions (see Figure 29), an optimal O_2 SR can be obtained.

In the following literatures, various controllers are designed to fulfill the abovementioned two control objectives simultaneously. Gruber *et al.* (2008) proposed a hierarchical control structure in order to regulate the O_2 SR. The master controller calculates the desired air flow for the slave controller in order to stabilize the O_2 SR at a fixed set point. In master controller, NMPC (nonlinear model-based predictive controller) is used.

In the salve controller, a nonlinear PI algorithm is used. Wendeker *et al*., 2007) tried to find and hold the maximum value of net power produced by the fuel cell stack through air flow control. In this chapter, an adaptive extreme control with biparameter identification was applied. Danzer *et al*. (2008) addressed O_2 starvation as well. A lumped air supply model was proposed to capture the cathode pressure and O_2 SR dynamically, which was achieved by developing an equivalent circuit diagram for pneumatic system using analogies to electrical system. As the system is nonlinear, flatness-based control techniques are applied.

Al-Durra *et al*. (2007, 2010) focused on the air/fuel supply system in tracking both optimum pressure and air flow, in order to achieve maximum system efficiency during load transients. In this literature, several multivariable control methods were compared: (1) linear control (observer-based, LQR, feedforward), (2) gain-scheduled control, and (3) rule-based control. Rgab *et al*. (2010) proposed three different feedforward methods: (1) lookup table based, (2) fuzzy logic, (3) neural network; the PID controller acted as feedback controller. It is concluded that the neural network feedforward plus PID feedback structure is better than the other two. Tekin *et al*. (2005) also applied PID control for the air supply. In order to reduce the parasitic power consumption by compressor motor, optimization of the several parameters was carried out with particle swarm optimization (PSO) algorithm. The main objective of Talj *et al*. (2009, 2010) is to propose a methodology to tune the air supply controller with

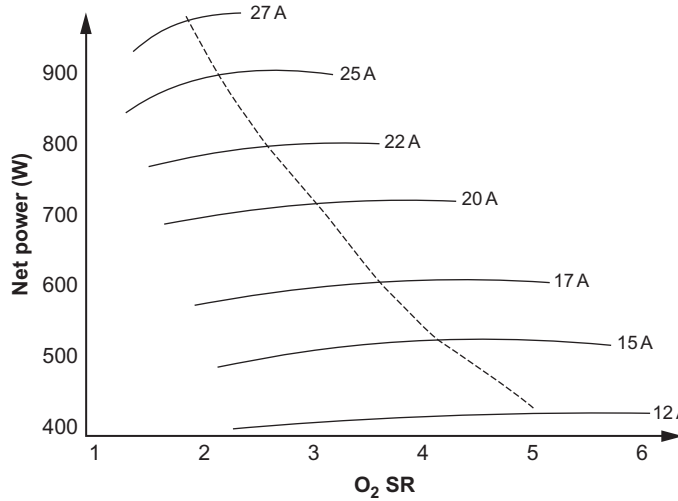

Figure 29 Typical relationship between O_2 SR and net power of the fuel cell system under varied load current conditions.

guaranteed stability properties. Some passivity and finite L2-gain properties were used to find a space for tuning controller parameters and to prove the stability of the interconnected controlled system.

3.3.1.2 Air management with current regulations The following literatures are concerned about the current regulation in the air management. The current load is regulated through a DC/DC converter, in order to avoid oxygen starvation. In the literature (Sun and Kolmanovsky, 2005), by regulating the current, the pointwise-in-time constraints on the O_2 SR and mass were strictly enforced to protect the fuel cell from O_2 starvation. The load governor was designed using a nonlinear reference governor (RG) approach. Taking both power following and oxygen starvation into consideration, the control of the current is aimed to do the following: (1) the applied load current tracks the demanded load current as close as possible; (2) the main constraints are satisfied for all the time. Thus, the demanded current can not be directly used as the reference input, but should be modified properly, and the corresponding strategy will be detailed sequentially Danzer *et al.* (2009) also used the MPC in their study to prevent O_2 starvation. This study presented a decoupled approach, where the effective fuel cell current was chosen as a controllable variable. In order to make the current drawn from the DC/DC converter achieve the desired current in a smooth manner, an exponential reference trajectory was applied as

$$I_{\text{ref}} = I_{\text{desired}} - (I_{\text{desired}} - I_{\text{drawn}}) \exp\left(-\frac{t}{\tau_{\text{ref}}}\right) \tag{79}$$

In the literature (Vahidi *et al.*, 2007), the goal of this study was to develop a computationally efficient load governor which prevents the compressor surge/choke, as well as O_2 starvation. In principle, two different strategies have been used for design of RG: (1) based on the MPC and the problem as an optimization issue, that is, the difference between the reference command and actual value is minimized over a future horizon and subject to pointwise-in-time constraints (Bemporad, 1998), (2) based on characterizing a set of initial conditions and references that would satisfy the constraints. Because of the reduced online computation, the governor is called a fast reference governor (FGR; Gilbert and Kolmanovsky (1999)). In this study, the FGR was applied. The design method was using a discrete-time linear model, and the reference modification can be accomplished via a first-order linear filter with a scalar adjustable bandwidth parameter β:

$$I_{\text{fc}}(k+1) = I_{\text{fc}}(k) + \beta(k)(I_{\text{d}}(k) - I_{\text{fc}}(k)) \tag{80}$$

where $\beta(k)$ belongs to [0,1]. To get so-called optimal $\beta(k)$ at each sampling time subject to the constraints, there are different ways. It can be arranged as an LP (linear program) problem with single variable $\beta(k)$ and

constraints for a certain horizon. Bisectional search for maximum is another way. Such online method is not suitable for real-time control. In the literature (Vahidi *et al.*, 2006), the objective of this control approach was to prevent O_2 starvation, air compressor surge/choke, and match an arbitrary level of current demand. The demanded current is managed between the fuel cell stack and energy buffer (ultra capacitor).

3.3.2 Case studies of air management

In the control of air supply in PEMFC system, also called air management, O_2 SR is commonly used as the controlled variable because it can affect the system efficiency or net output power (see Figure 29). For a specific PEMFC system, there exists a static relationship which describes how the O_2 SR influences the system efficiency or net power under a given required current condition. Such relationship obtained experimentally or by the model-based technique can be used to determine the optimal O_2 SR (set point) for the corresponding controller. According to the survey of air management, there are two strategies: without current regulation and with current regulation. In the following, two cases are studied addressing both strategies.

3.3.2.1 Case 1: Control of O_2 SR Typically, the current is treated as a measureable disturbance in the O_2 SR control strategy. Figure 30 is the control block diagram for O_2 SR. In this figure, the reference O_2 SR is obtained by the set point generator which contains the prementioned static relationship. The O_2 SR is selected as the controlled variable, and the air mass flow rate at the stack inlet is treated as the manipulated variable which is influenced by the control voltage of compressor motor. The control objective is to maintain the O_2 SR at the optimal value and reject the impacts from the external disturbance. To achieve such objective, the feedback+feedforward controller is used in this case. The feedforward controller speeds up the response of the system and the feedback controller try to reduce the difference between the controlled variable and set point, as well as to stabilize the system. For the sake of simplicity, the PI controller is applied as the feedback controller. The parameters of the PI controller are determined heuristically. The model of the PEMFC system has been already described in the previous chapter and will not be discussed here.

Figure 31 shows the driving cycle of the required current. Depending on the static relationship, the optimal O_2 SR in this case is selected as 5.0 when the required current is smaller than 100 A, and 2.0 when the current is larger than 100 A. Consequently, a step change of reference O_2 SR is obtained through the set point generator in the simulations. Figure 32 shows the set point change and the controlled O_2 SR. It can be found that the O_2 SR can be controlled well. The fluctuations of O_2 SR are caused by

the required current changes. This is because the rate of electrochemical reaction is quite fast and the flow rate of air feeding into the stack is considerable slow. Two PI controllers are compared in Figure 32. It is found that larger proportional coefficient in PI controller can speed up the system response but can cause more oscillations.

Figures 33–35 show the selected variables regarding the voltage of compressor motor, air-flow rate at the stack inlet as well as compressor speed. In Figure 33, the PI controller with large proportional coefficient generates higher peak values in the control signal of compressor motor. Figures 34 and 35 do not show the obvious differences between the two PI controllers.

3.3.2.2 Case 2: Control of the O_2 SR fluctuations with current regulation In Case 1, a deep decrease or increase in the O_2 SR occurs when the current is changed instantaneously into a higher or a lower value. Such fluctuation can bring negative influences on the lifetime of the PEM fuel cell stack (Mitsuda and Murahashi, 1991). Hence, in case of the instantaneous change of current, the current regulation concept could be employed to reduce the fluctuations on the O_2 SR. In this case, the current is controlled by using an open-loop structure which means there is no current feedback loop because the current can be regulated by a DC/DC converter in a considerable fast way. Figure 36 shows the O_2 SR fluctuations' control by means of manipulating current. A current regulation block is added based on Figure 30.

In this case, the current is not changed instantaneously into the required current, but with a transient profile of first-order process. The shape of such profile is influenced by the selected time constant. In order

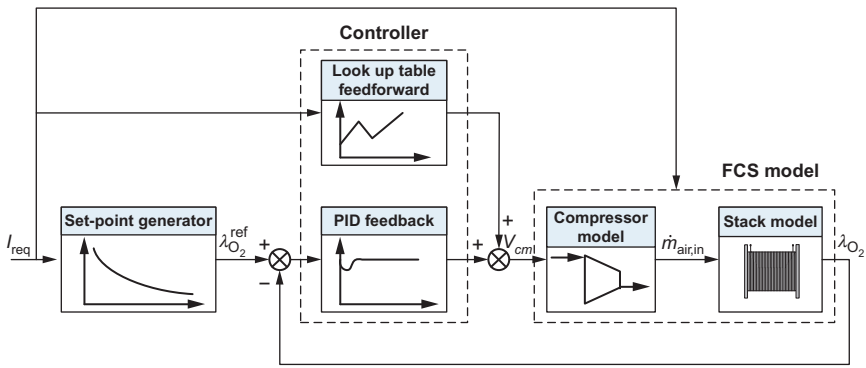

Figure 30 Control block diagram for O_2 SR.

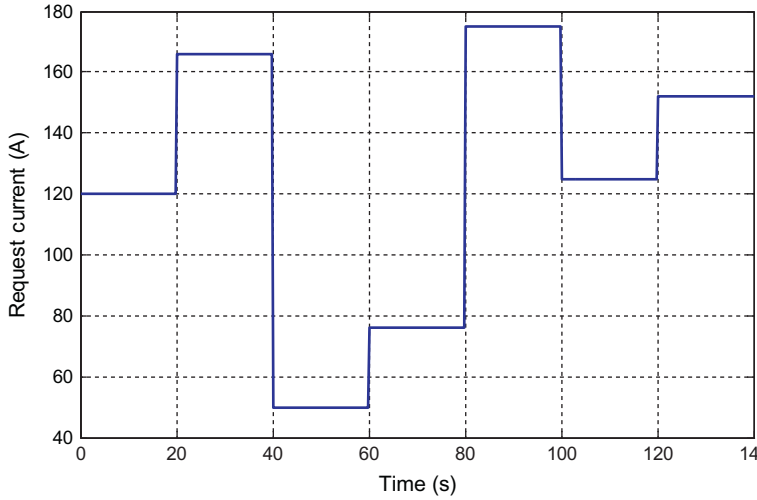

Figure 31 Load cycle of the required current.

to describe the O_2 SR fluctuations quantitatively, an index function J is introduced:

$$J = \frac{\int_0^{T_s} \left|\lambda_{O_2} - \lambda_{O_2}^*\right|^2 dt}{T_s} \tag{81}$$

where λ_{O_2} is the real O_2 SR, λ_{O_2}* is the optimal O_2 SR, and T_s is the simulation time. In Figure 37, it is observed that there is an optimal time constant (about 0.07s) with respect to the minimum J.

In order to test this case, the corresponding simulations are carried out. For comparison to Case 1, the identical load cycle in Figure 31 is applied during the simulations. Figure 38 shows two scenarios of the load current. In the zoomed region, the regulated current varied slightly slower than the unregulated one. Figure 39 shows the O_2 SR with current regulation. For comparison, the O_2 SR in Case 1 is combined into Figure 39 as well. It is observed that the fluctuations on O_2 SR are sufficiently reduced.

Summarizing, for the air management in the PEM fuel cell system, there exist two strategies: without current regulation and with current regulation. In the first strategy, the current is treated as a measurable disturbance, and usually, a feedforward+feedback control structure is applied (see Figure 30). In the second strategy, the current is controlled by means of a first-order open-loop controller (see Figure 36). The

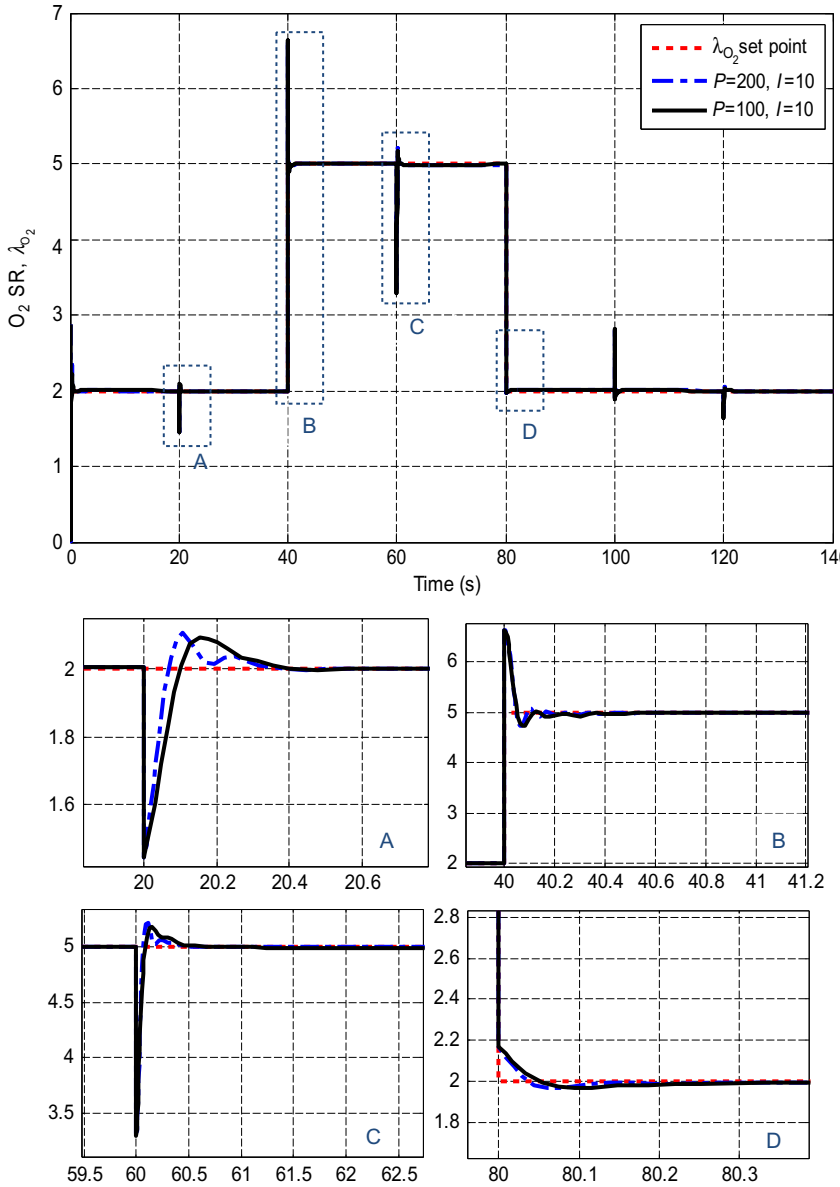

Figure 32 O_2 SR and its set point.

fluctuations on O_2 SR are reduced by choosing an optimal time constant in the current controller.

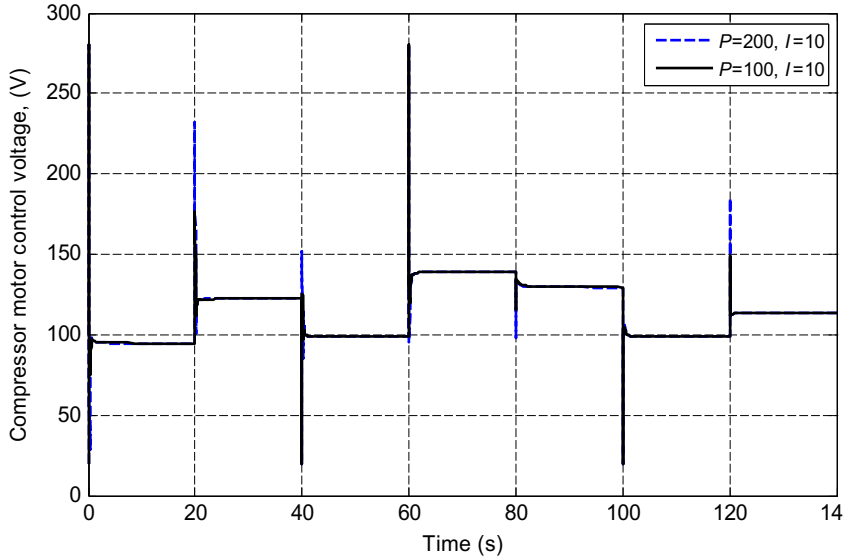

Figure 33 The profile of compressor motor voltage.

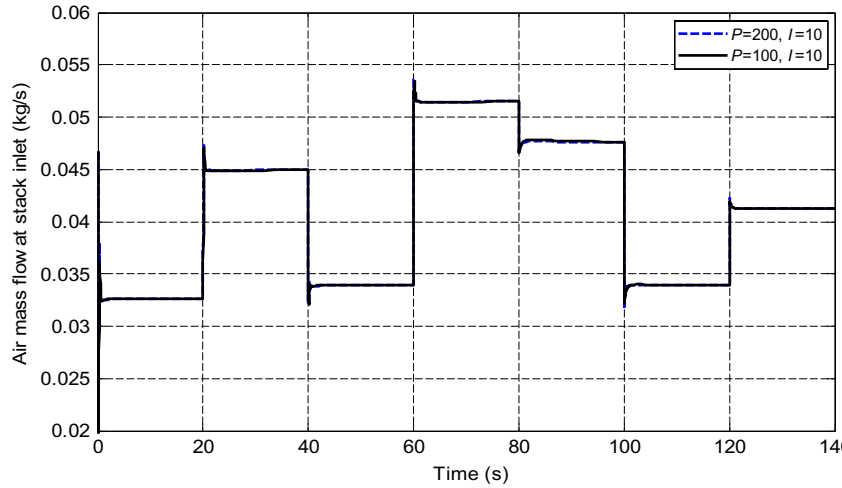

Figure 34 The profile of the air-flow rate at the stack inlet.

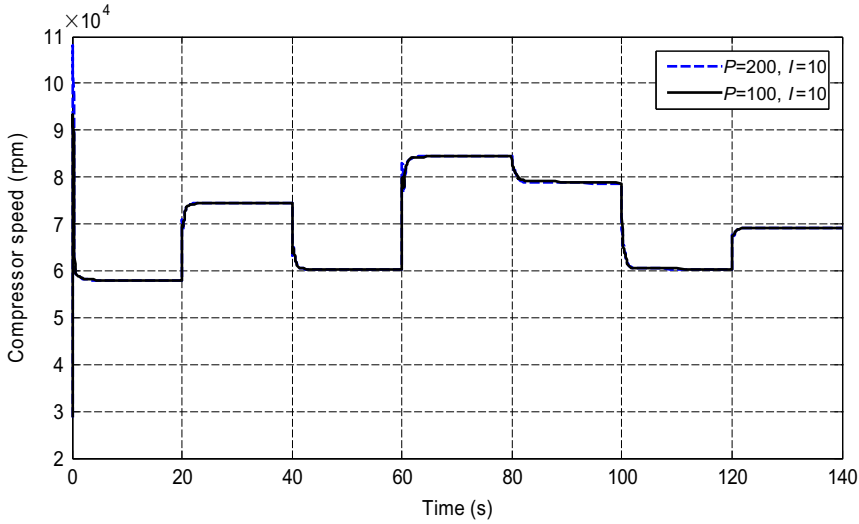

Figure 35 The profile of the compressor speed.

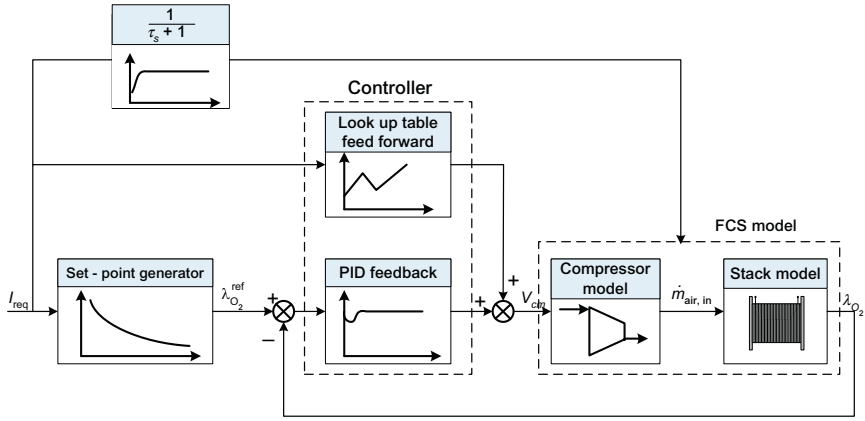

Figure 36 The O_2 SR fluctuations control by means of manipulating current.

3.4 Introduction of PEMFC fault diagnosis technology

3.4.1 General introduction

In order to ensure the quality, performance, and safety of PEMFC system, fuel cell diagnosis has become an essential detecting technique and developed rapidly in recent years (Wang *et al.*, 2007). Currently, in fuel cell

diagnosis field, CVM technology is the most widely applied. The principle of CVM is to detect the faults of the fuel cell via measuring each single (or a pair)-cell voltage. As shown in Figure 40, it is a typical arrangement of CVM hardware relative to the fuel cell stack. The influences of temperature, humidity, and air mass flow, etc. could be analyzed by CVM method. However, where up to several hundreds of voltage channels have to be measured; CVM method greatly increases the wire connection, operational complexity, and instability (Brunner *et al.*, 2010; Webb and Moller-Holst, 2001).

For the drawbacks of CVM technique, AVL List GmbH has developed an innovative solution, which is named total harmonic distortion analysis (THDA). The principle of THDA is, according to the analysis of total output voltage in real time, diagnosing the operational status, safety, and reliability of fuel cell system. In practice, by adding a small amplitude signal with specific frequency pattern to the fuel cell system, if for some critical operations causing the voltage changing in one single cell or cells, the response will be distorted in the frequency domain. Then, through a series of output curve analysis, such as wavelet analysis, the fault types can be identified and reasonable measures will be adopted. For instance, when a critical cell operation occurs, if, for example, low air stoichiometry causes a sharp drop of cell voltage at a certain current, as the current is

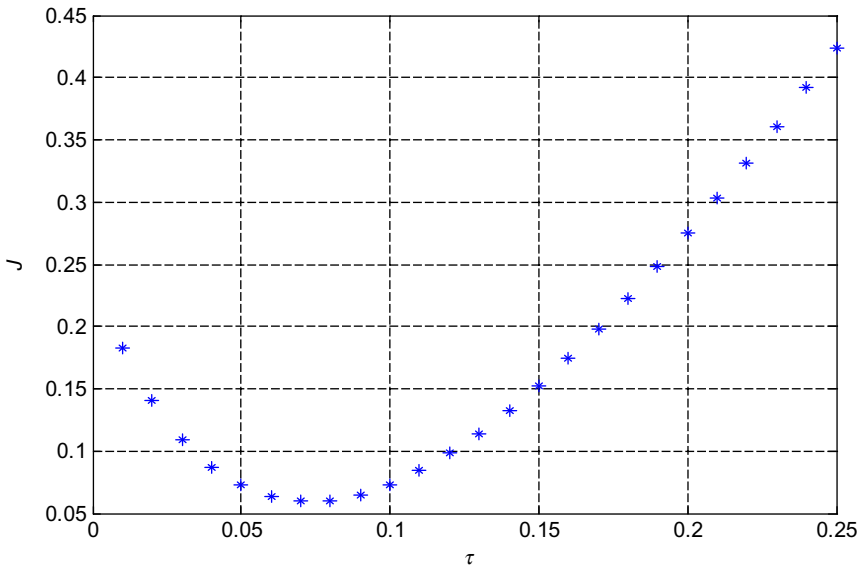

Figure 37 The relation between the cost function and time constant under a given load cycle.

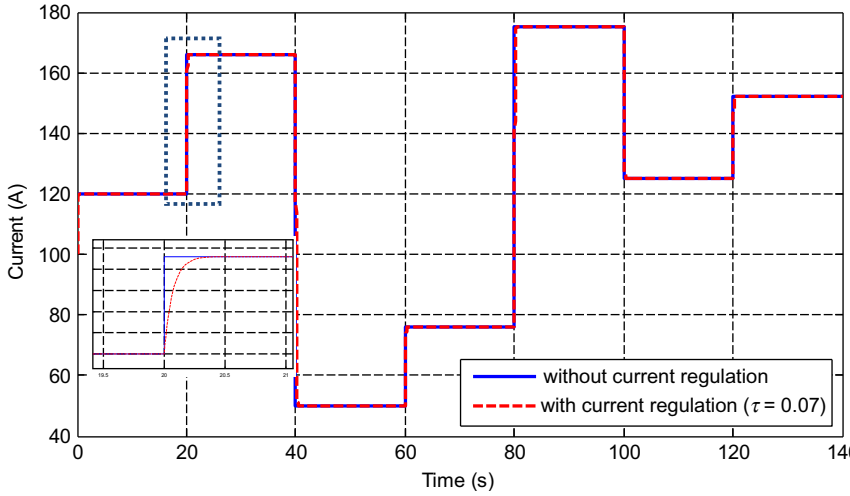

Figure 38 Regulated current cycle.

superimposed by a small amplitude signal with specific frequency pattern, then it will cause distorted frequency fractions extractable from the entire stack voltage (Ramschak *et al.*, 2006).

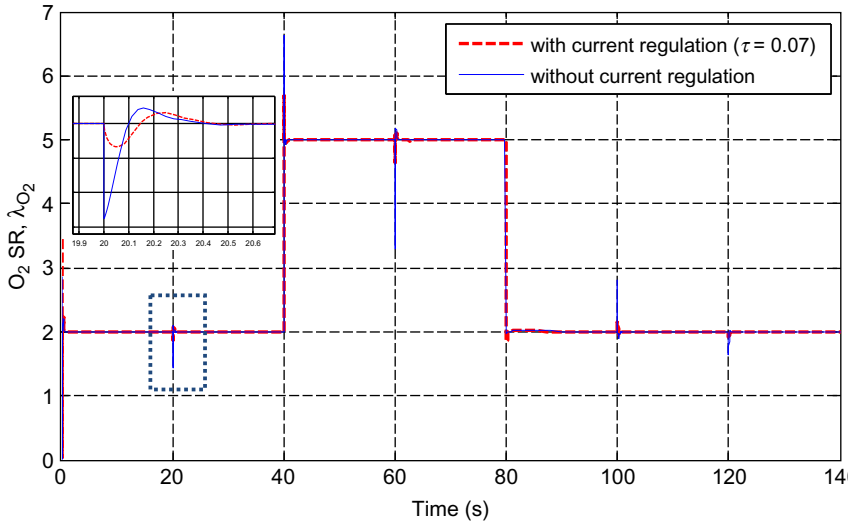

Figure 39 The profiles of O_2 SR with and without current regulation.

3.4.2 CVM

3.4.2.1 Hardware structure As well known, every single fuel cell will directly affect the operation state of entire fuel cell stack. Therefore, real-time monitoring for single-cell voltage is needed. This section reviews the CVM technique by introducing mainly a specific CVM system in a 5-kW PEMFC stack (Wu *et al*., 2008). The structure of the CVM system will be described in the following.

A single piece of fuel cell can produce about 1V voltage at maximum. In order to provide required voltage to the load, the cells need to be stacked. The monitoring for single-cell voltage can timely detect the abnormal conditions and take the corresponding troubleshooting measures or change the operation strategy, thereby protecting the fuel cell stack and prolonging the lifetime. When fuel cells convert from standby state (stack current $I=0$) to the working state ($I>0$), it will produce the change of fuel cell voltage and electrode potential, namely, the polarization phenomenon. This phenomenon can indicate the energy loss to a certain extent when fuel cells convert from standby state to the working state. Usually, by inspecting the fuel cell voltage and current, a real-time polarization curve (U–I curve) can be obtained. The curve can be used for the fuel cell system feedforward control strategy, such as the setting of required air amount and corresponding working pressure.

A typical U–I curve, as shown in Figure 41, is divided into three areas. The first area is the activation polarization area; the second is the Ohm's polarization area, which is caused by fuel cell internal resistance including membrane resistance, electrode resistance, and various contact resistances. In such area, the voltage change with current is close to linear and the normal operating area is in this area as well; the third is the concentration polarization area, which is caused by the reactants transport

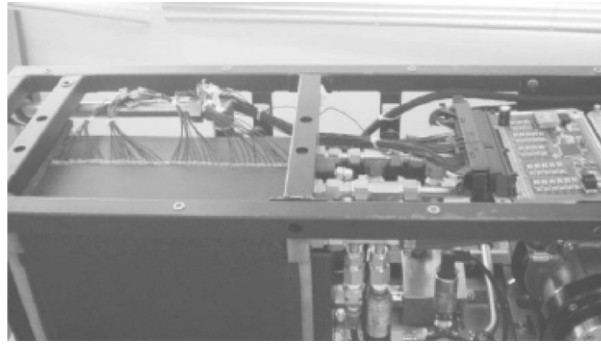

Figure 40 Typical arrangement of CVM system relative to the fuel cell (Mulder *et al*., 2008).

limitation in the gas diffusion layers under the large current condition (Yi, 2003).

Figure 42 shows the connection among the CVM system, fuel cell stack as well as FCU (Fuel Cell Control Unit). CVM system collects single-cell voltages periodically by using the metal PIN stitches inserted in the bipolar plates. Then, the data need to be processed (such as the calculations of maximum voltage, minimum voltage, and total voltage). After that, the results are transferred to FCU by CAN bus. FCU will do the corresponding fault treatments based on the predefined criterion (such as turn off the system in emergency or send the demand of decreasing the current). As shown in Figure 43, the hardware structure of the exemplary CVM system includes the voltage division circuit, differences amplifier, A/D converter, single chip microcontroller (SCM), and CAN circuit. These components are connected electrically. In this CVM system, there are 45 measuring channels (each measuring channel detects two pieces of single cells), which are divided into four groups A, B, C, and D. Groups A, B, and C have 11 measuring channels for each one. The monolithic voltage signals are collected and input to three A/D transforming chips (with 11 channels for each one) separately according to these measuring channels. Then, the converted data are sent to SCM by serial peripheral interface (SPI). Group D has 12 measuring channels.

Before the data delivery, the collected voltage signals need to be preprocessed. First, the electrical signal transits into the voltage division circuit because the signal passed through the voltage division circuit has small amplitude and needs to be amplified. For each measuring, one channel detects two pieces of single cells, and the maximum detected voltage is

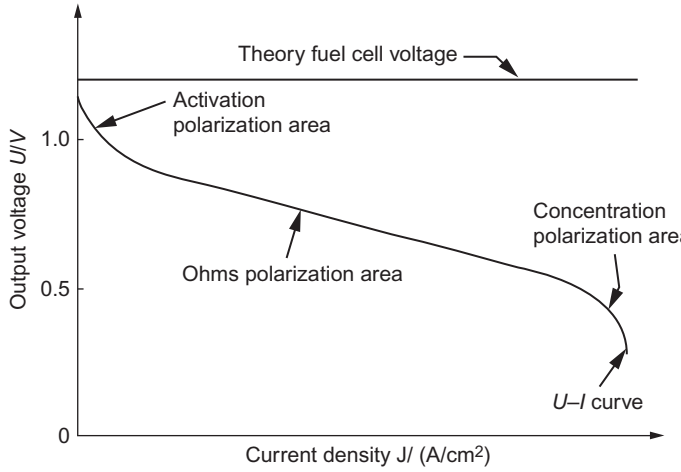

Figure 41 *U–I* curve of the fuel cell.

2V. Afterward, the amplified signal will be sent to the A/D transforming chip. In order to ensure the effective electrical isolation between different groups, the design of source module needs to be carefully considered.

3.4.2.2 Software design The software design of CVM system is based on the SCM, for example, MC9S12DP256 microcontroller. The main framework of the software are divided functionally by executive order into three steps: 1) program initialization; 2) read the voltage data from ADC and do some relevant calculations; 3) send the processed signal to the FCU through the CAN bus. There are two types of data transferring on the CAN bus: one is the trigger signal from the FCU to CVM system and the other is the cell voltage data. For the purpose of sending trigger information to FCU, the program adopts the method of timer overflow interrupt. In the process of interrupt handling, the FLAG value needs to be read, and then the transmit mode is chosen. The flowchart of timer interruption program is shown in Figure 44.

3.4.3 Total harmonic distortion analysis

3.4.3.1 Harmonic distortion analysis approach To understand the harmonic distortion theory, three concepts must be introduced: harmonics, fundamental harmonic, and total harmonic distortion (THD). The word 'harmonics' originates from acoustics field. A harmonic of a wave is a component frequency of the signal that is an integer multiple of the fundamental frequency, that is, if the fundamental frequency is f, the harmonics have frequencies $2f$, $3f$, $4f\ldots$, etc. The harmonics have the property that they are all periodic at the fundamental frequency.

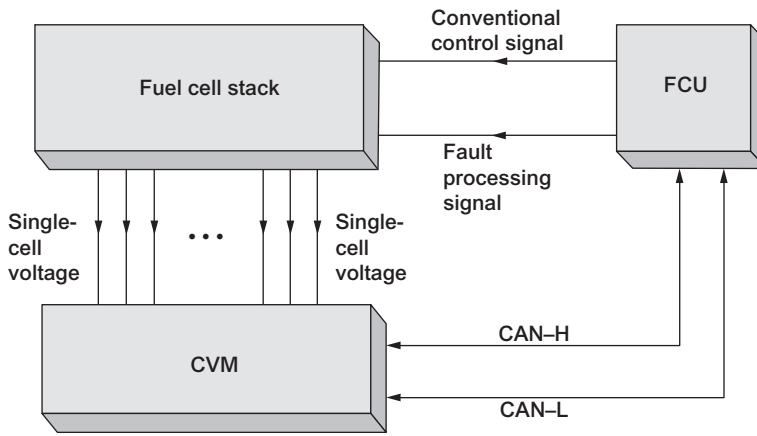

Figure 42 Operational scheme of CVM system.

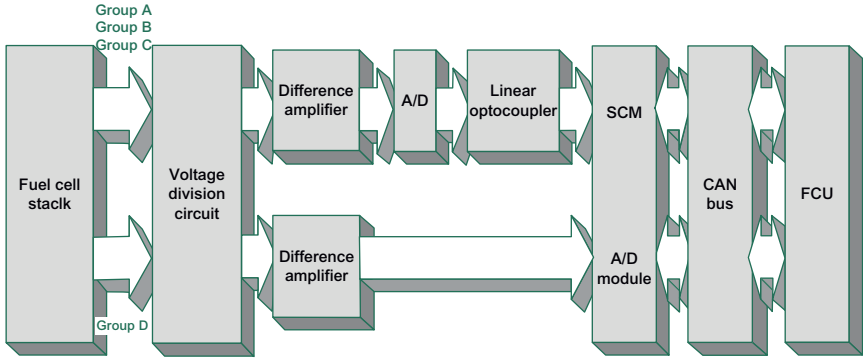

Figure 43 Hardware structure of exemplary CVM system.

Therefore, the sum of harmonics is also periodic at that frequency. Harmonic frequencies are equally spaced by the width of the fundamental frequency and can be found by repeatedly adding that frequency. For example, if the fundamental frequency is 60Hz, the frequencies of the harmonics are 120, 180, 240Hz, etc. The fundamental frequency, often referred to simply as the fundamental and abbreviated $\mathbf{f_0}$ or $\mathbf{F_0}$, is defined as the lowest frequency of a periodic waveform. The THD of a signal is a measurement of the harmonic distortion present and is defined as the ratio of the sum of the powers of all harmonic components to the power of the fundamental frequency.

To understand a system with an input and an output, such as an audio amplifier, we start with an ideal system where the transfer function is linear and time invariant. When a signal passes through a nonideal, nonlinear device, additional content is added at the harmonics of the original frequencies. THD is a measurement of the extent of that distortion.

$$\mathrm{THD} = \frac{\sum \mathrm{Hp}}{\mathrm{Fp}} = \frac{\mathrm{Vh}}{\mathrm{V}_1} = \frac{\sqrt{\left(V_2^2 + V_3^2 + \cdots + V_n^2\right)}}{\mathrm{V}_1} \tag{82}$$

where $\sum$Hp is the set of harmonic energy, Fp is the fundamental frequency energy, Vh is the root mean square of the harmonics, and V_1 is amplitude of fundamental frequency.

3.4.3.2 Detection of fuel cell critical status by stack voltage analysis
Because of the serial connection of hundred cells in a fuel cell stack, the critical operation of even just one cell can cause the failure of the whole stack and accordingly shorten lifetime or reduce the reliability. The

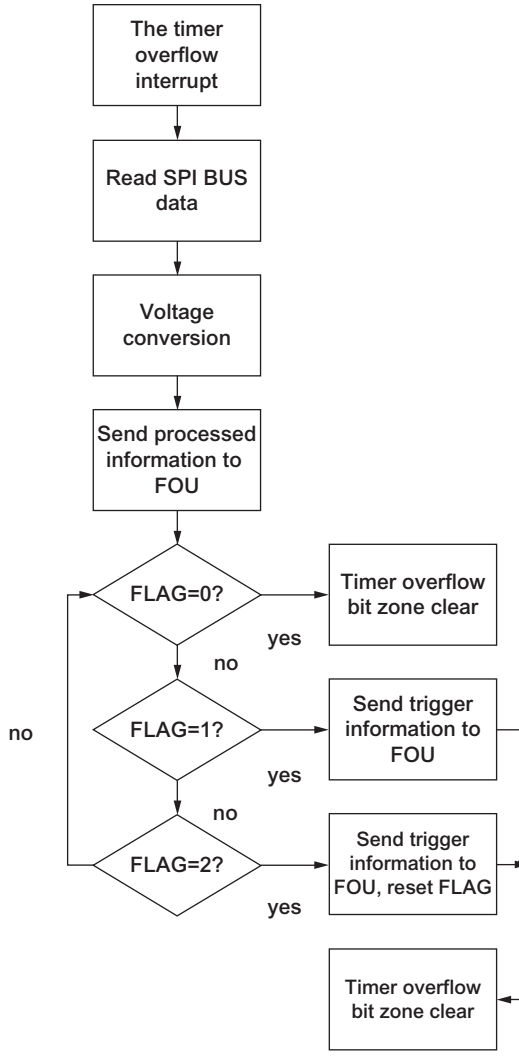

Figure 44 The flowchart of timer interruption program.

traditional CVM method detects the possible failure of a cell by measuring all voltages of every single cell or every pair of cells. The requirements of wiring and instrumentation are extremely large. Therefore, the cost is relatively high and the operation is complicated. In contrast, THDA approach can monitor stack status and identify the fault in real-time from the sum voltage barely.

In the fuel cell operation of the new approach by AVL List GmbH, a small amplitude sinusoidal current signal is superimposed continuously to the stack current, which connected in parallel to the fuel cell operating point. As the cell transfer function within the usual operation range, such as *U–I* curve, is linear, the responding cell voltage signal consists of the same frequency spectrum as the original superimposed one.

The formed harmonics, which are caused by critical operating conditions, were detected in the frequency spectrum of the entire stack voltage, even if only a single or few cells generate harmonic distortion and therefore extra spectral contents. The spectral content of the measured voltage signal is correlated with the spectral content of the superimposed current signals. Deviations are analyzed and evaluated in terms of critical fuel cell status.

Figure 45 shows in principle the distortion of a sinusoidal current signal when an actual operating current is either at a critical (solid curve) or at a typical normal (dashed–doted curve) condition. Generally, harmonic distortion occurs at conditions with insufficient air or hydrogen supply at mass transport limitations or even during cell voltage drifts or temporary drops caused by other reasons (Ramschak *et al.*, 2006).

In Figure 46, the hardware schematic of THDA device is described. An auxiliary signal source is adding a small amplitude alternating current (AC) signal to the system. With a capacitor, the AC signal is shifted to the usually high DC (direct current) level of the stack voltage. On average, the stack output power is not influenced by this device. The stack is loaded and unloaded adequately to the superimposed current (rule of Kirchhoff, refer to Figure 46: $IB_{STACK}=IB_{LOAD}-IB_{THDA}$). The sinks for the AC signal are the external loads and system auxiliaries.

At steady state of the fuel cell system, only the measurement of the sum voltage of up to several hundred cells is required. At transient conditions, the additional measurement of the current is needed in order to compensate the spectral impact of sharp load changes. Only the AC part of the stack voltage is measured (high-pass coupling), and the full dynamic range of the analogue digital converter (ADC) can be utilized for the analysis of the AC signal content. Furthermore, the measurement, denoising, and transformation of the signals into the time–frequency or frequency domain with the subsequent analysis can be implemented by an embedded digital signal processor (DSP) board.

3.4.4 Research methods and main challenges

Currently, CVM technique is the most widely used method in fuel cell diagnosis. However, as up to several hundreds of voltage channels have to be measured, CVM greatly increases the wire connection, operational complexity, instability, and the cost. THDA technique can dramatically

reduce the contacting and cost by only measuring the stack total voltage. The new approach can effectively diagnose several main critical stack operation modes, such as insufficient air supply, low hydrogen stoichiometry, fuel cell membrane dry, and water flooding.

Additionally, one of the advantages of THDA technology is that the signal can be put into the frequency domain for its spectrum components analysis, which greatly reduces the effects of the electromagnetic interference. However, in the analysis of the results, the technique still has some problems to be further studied, which is also the difficult points, such as de-noising, the influence of instantaneous load changing, the effects of the electromagnetic influence, the influence of converter and inverter. Thus, some new methods must be brought forward to solve these tough problems.

Nevertheless, THDA can hardly confirm the exact fault location. In this case, wavelet analysis could be employed to deal with the problem. In the course of the harmonic analysis, wavelet analysis will be the main method for study. In frequency domain, Wavelet analysis has become a foundation as the same as Fourier analysis. Also, wavelet theory is more suitable for signal with time-varying, broadband noise or frequency varying. The wavelet transform, which has the characteristics of different scales/resolution, will do the multiscale decomposition for the detected output signal and, then by the respective processing, reconstruct the signal without any interference.

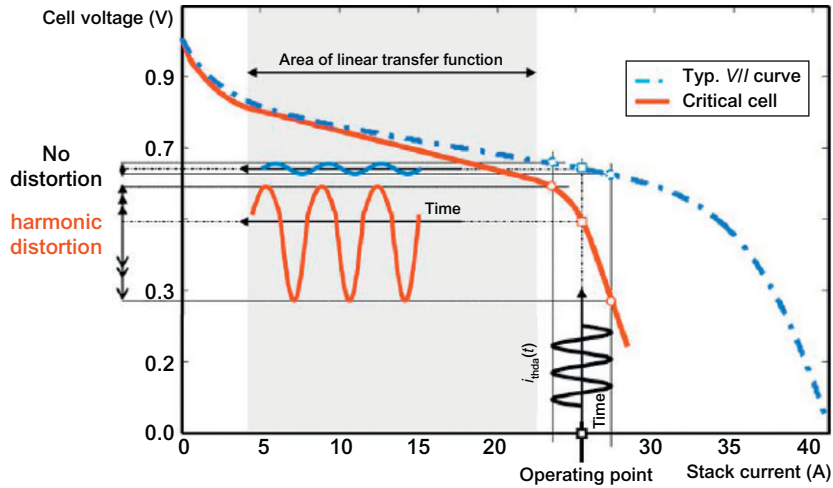

Figure 45 Distortion of a sinusoidal signal (principle) (Ramschak *et al*., 2006). (Approved by the copyrights owners of Ramschak *et al*. (2006).)

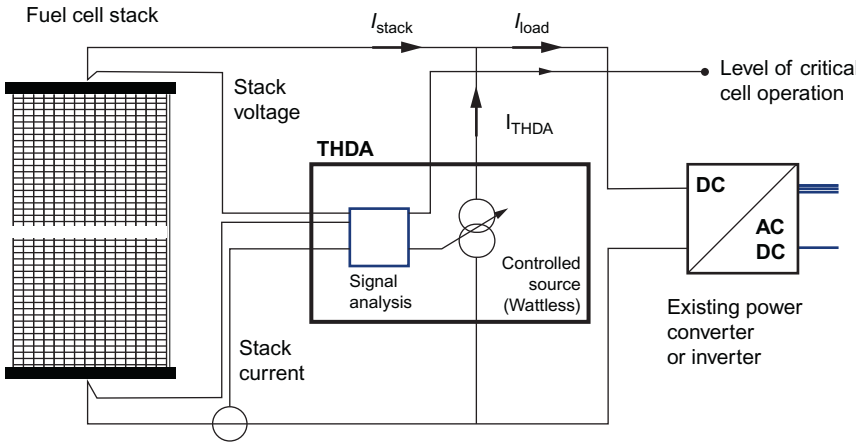

Figure 46 Hardware realization of the AVL THDA (Ramschak *et al*., 2006). (Approved by the copyrights owners of (Ramschak *et al*., 2006.)

The main challenges for fuel cell fault diagnosis in the future can be drawn as: first, fault location algorithm will be study via THDA. Second, it is the combination of CVM and THDA method. Additionally, the analytical method and more types of faults diagnosis studies still have ample room to be improved.

4. SUMMARY AND CONCLUSIONS

The PEMFC system modeling and control are critical for the system integration and safe operation. To better understand the system behaviors, two kinds of the models, that is, the lumped and distributed parameter models, are developed. In the development of the lumped parameter model, an engineering oriented modeling method is employed to capture the transient processes in the PEMFC system. The corresponding results show that the model can be sufficient to represent the real system by means of the *U–I* curve and dynamic profiles. Based on the model, analysis of the parameter sensitivity is carried out as well (see Figures 8–10). In the development of the distributed parameter model, the CFD is used to model the fuel cell stack, and the auxiliary units are modeled with lumped parameter models. The 3D CFD stack model is implemented in Fluent package, and others are realized in Matlab/Simulink environment. The collaborative simulations with Fluent/Simulink are carried out to investigate the internal phenomena when the stack boundary conditions (e.g., inlet humidity, flow rate) are changed by the specific controller, for example, the

spatial distributions of the characteristic variables (such as temperature, current, hydrogen, oxygen, and water). Additionally, the proposed collaborative platform can overcome the drawbacks of both lumped parameter model and distributed parameter model. The collaborative simulation platform can be used for the following purposes: (1) matching estimation of the auxiliary units and stack; (2) a useful diagnostic tool. For example, we can investigate the stack based on the polarization curve, current interrupt, pressure drop, and current density mapping, which can be all obtained from the collaborative simulation platform; (3) the optimization design of PEMFC systems.

The hydrogen purge, thermal management, and air supply are selected in this chapter as three control issues. As for the hydrogen purge, two parameters (purge cycle T and purge duration time ΔT) are selected to be optimized in order to obtain higher efficiency. It is observed experimentally that the maximum cycle is 40s for the given stack. The purge duration time is critical for the hydrogen utilization ratio and efficiency. This value is determined by minimizing a predefined cost function. As for the thermal management, two control algorithms are carried out and compared. It is noted that the thermal management for the PEMFC system is typically a systematical problem in that it includes not only the stack cooling issue but also the cathode gas cooling. Normally, the air temperature out of the air compressor is over 100°C, and the hot air needs to be cooled down, in order to reduce the humidifying load. As for the air supply, a comprehensive review is made. Two cases for the air supply, that is, without and with current regulation, are studied. In the first case, the current is treated as a measurable disturbance. A feedforward+feedback control structure is applied to control the oxygen stoichiometry. The oxygen stoichiometry fluctuation cannot be avoided. In the second case, the concept of current regulation is introduced to reduce the oxygen stoichiometry fluctuation. Additionally, two PI controllers with different proportional coefficients are implemented and compared.

As well known, the monitoring function is widely embedded in the control system. In order to avoid of the failures inside of the fuel cell, the diagnose technology is required. In this chapter, the CVM method is, first, introduced because this method is frequently used in the fuel cell stack in the automotive application. It is also pointed out that such method can lead to the wiring issues. Instead of the CVM, the THDA technique proposed by AVL GmbH is described as an example. This method only measures the stack voltage instead of single-cell voltages.

NOMENCLATURE

A	area, m^2
C	valve flow coefficient
C_P	specific heat, J/(molK)
D_w	water diffusivity in the membrane, m^2/s
E	open circuit potential/energy, V/J
F	faraday constant, 96,487C/mol
i	current density, A/cm^2
I	current, A
j	molar flux, $mol/(sm^2)$
k	thermal conductivity, W/(mK)
K	hydraulic permeability, m^2/s (or, ratio)
Kr	gear ratio
L	length, m
m	mass, kg
$\dot{m}$	mass flow rate, kg/s
M	molar weight, mol/kg
n	amount of mole
$\dot{n}$	molar flow rate, mol/s
N	amount
P	pressure, atm.
PW	power, W
Q	heat, J
$\dot{Q}$	heat flux, J/m^2
r	latent heat of vapor, J/kg
rpm	revolutions per minute, N/min
R	universal gas constant, 8.314J/(molK)
t	time, s
T	temperature, K
Tq	torque, Nm
$\overrightarrow{u}$	superficial velocity, m/s
U	voltage, V
V	volume, m^3
X	mole fraction of species
Y	mass fraction of species
α	heat dissipation coefficient
β	coefficient
χ	humidity ratio
ε	porosity
η	over potential, V
φ	relative humidity
κ	ratio of specific heat
λ	coefficient (or water content)

μ	viscosity, kg/(ms)
ρ	density, kg/m^3
σ	conductivity, S/m
τ	time constant, s (or, viscous stress, N/m^2)
ω	angular velocity
ξ	coefficient
ζ	stoichiometry flow ratio

SUPERSCRIPT

AfterPump	after pump
Inc	intercooler
Max	maximum
outFC	out of the fuel cell
outInc	out of the intercooler
pump	pump
req	required
stack	stack
SUM	summation
ToFC	into the fuel cell
ToInc	into the intercooler

SUBSCRIPT

a	anode
act	activator
air	air
amb	ambient
amp	ambient pressure
back	feedback
bpv	back pressure valve
c	cool/cathode
cell	single fuel cell
ch	channel
comp	compressor
conc	concentration
cons	consumption
conv	convection
coolant	coolant
drop	pressure drop

el	electric
exp	expander
fr	friction
fuc	fuel cell control unit
g	gas
gross	gross
H_2	hydrogen
H_2O	water
hum	humidifier
in	inlet
Inc	intercooler
l	liquid
late	latent
melt	melting point
mem	membrane
mot	motor
N_2	nitrogen
O_2	oxygen
ohm	ohmic
out	outlet
para	parasitic
Pr	pressure ratio
prod	product
rad	radiator
ref	reference
sat	saturation
sol	solid
st	stack
std	standard condition
sur	surface
temp	temperature
val	valve
ve	vessel
veh	vehicle
weg	wet gas

LIST OF SYMBOLS

$\cong$	approximately equal
$<$	less than
$\sum$	summation
$\longleftrightarrow$	equivalent to, if and only if

$\bar{T}$	the average of the variable T
$\partial f/\partial t$	the partial differential of f with respect to t
$\int_0^t f(t)\mathrm{d}t$	the integral of the function *?f* from 0 to t
$\nabla\cdot(\vec{u})$	the gradient vector
ΔF	the variation of a variable F
$\leq(\geq)$	less (greater) than or equal to
$\lvert a\rvert$	the absolute value of a scalar a
$L^{-1}(\ )$	the inverse Laplace transformation
Max	maximum
S→P	a map from a set S to a set P

ACKNOWLEDGMENTS

The authors appreciate the Chinese National 863 project of ''High-temperature PEMFC System Evaluation.'' Additionally, the authors give their thanks to Dr. Sun Pengtao (University of Nevada, Las Vegas, USA) due to the inspiring discussions on the numerical CFD solving techniques. Finally, the authors appreciate the students, Guangji Ji, Shuang Zhai, Kunpeng Gao, Fenglai Pei, Jichen Liu, Lan Zheng, Mingchao Ding, Yan Jiang, and Kan Wu, due to their contributions to this chapter.

REFERENCES

Ahn, Jong-Woo and Choe, Yong-Yu, *J. Power Sour.* **179**(1), 252–264 (2008).
Al-Durra, A., Yurkovich, S. and Guezennec, Y., *in* Proceedings of 2007 ASME International Mechanical Engineering Congress and Exposition (IMECE2007), Washington, USA, pp. 225–233. (2007).
Al-Durra, A., Yurkovich, S. and Guezennec, Y., *Int. J. Hydrogen Energy* **35**(20), 11291–11307 (2010).
Arce, A., Ramirez, D. R., del Real, A. J. and Bordons, C., *in* Proceedings of the IEEE Conference on Decision and Control, pp. 6088–6093. (2007).
Arce, A., et al. *IEEE Trans. Ind. Electron.* **57**(6), 1892–1905 (2010).
Bemporad, A., *Comput. Ind.* **36,** 55–64 (1998).
Brunner, D., Prasad, A. K., Advani, S. G. and Peticolas, B. W., *J. Power Sour.* **195,** 8006–8012 (2010).
Bussayajarn, N., Ming, H. Hoong, K. K., et al. *Int. J. Hydrogen Energy* **34,** 7761–7767 (2009).
Carlson, E. J., Kopf, P. Sinha, J., et al. ''Cost Analysis of PEM Fuel Cell Systems for Transportation''. www.nrel.gov/hydrogen/pdfs/39104.pdf (2005).
Cheddie, Denver and Munroe, Norman, *J. Power Sour.* **156**(2), 414–423 (2006).
Corbo, P., Migliardini, F. and Veneri, O., *Renew. Energy* **34,** 1955–1961 (2009).
Danzer, M. A., et al. *J. Power Sour.* **176,** 515–522 (2008).
Danzer, M. A., et al. *J. Power Sour.* **190,** 86–91 (2009).
Fabian, T., Posner, J. D. O'Hayre, R., et al. *J. Power Sour.* **161,** 168–182 (2006).
Frano, Barbir, ''PEM Fuel Cells: Theory and Practice''. Boston, Elsevier Academic Press (2005).
Gilbert, E. and Kolmanovsky, I., *Int. J. Robust Nonlin. Control* **9,** 1117–1141 (1999).

Gou, J., Pei, P. C. and Wang, Y., *J. Power Sour.* **162,** 1104–1114 (2006).
Gruber, J. K., Bordons, C. and Dorado, F., *in* Proceedings of 2008 American Control Conference, Washington, USA, pp. 1121–1126. (2008).
He, Mingyan, Zhou, Su, Huang, Ziping and Sun, Pengtao, *J. Syst. Simul.* **23**(1), 38–43 (2011).
Himanen, O., Hottinen, T. and Tuurala, S., *Electrochem. Commun.* **9,** 891–894 (2007).
Kolodziej, J. R., *J. Fuel Cell Sci. Technol.* **4**(3), 255–260 (2007).
Li, Xi, Cao, Guangyi and Zhu, XinJian, *J. Shanghai Jiaotong Univ. (Sci.)* **2,** 157–159 (2005).
McKay, D. A., ''Stack Level Modeling and Validation of Low Temperature Fuel Cells and Systems for Active Water Management''. (2008). Ph.D. Dissertation, University of Michigan, Ann Arbor, MI, USA.
McKay, D. A., Ott, W. T. and Stefanopoulou, A., *in* ''Proceedings of the 2005 ASME International Mechanical Engineering Congress Exposition'', volume 2005, 1177–1186. (2005).
McKay, D. A., Siegel, J. B. Ott, W., et al. *J. Power Sour.* **178,** 207–222 (2008).
Mitsuda, K. and Murahashi, T., *J. Appl. Electrochem.* **21**(6), 524–530 (1991).
Mokmeli, Ali and Asghari, Saeed, *Int. J. Hydrogen Energy* **35,** 9276–9282 (2010).
Mulder, G., Ridder, F. D., Coenen, P., Weyen, D. and Martens, A., *Int. J. Hydrogen Energy* **33,** 5728–5737 (2008).
Muller, E. A., Kolb, F. Guzzella, L., et al. *J. Fuel Cell Sci. Technol.* **7**(2), 0210131–02101311 (2010).
Peng, Hu, *Int. J. Hydrogen Energy* **35,** 9110–9123 (2010).
Pengtao, Sun, Guangri, Xue, Chaoyang, Wang and Jinchao, Xu, *in* Proceeding of Sixth International Fuel Cell Science Engineering and Technology Conference, 851–864. (2008).
Ramschak, E., Peinecke, V., Prenninger, P., Schaffer, T. and Hacker, V., *J. Power Sour.* **157,** 837–840 (2006).
Rgab, O., Yu, D. L. and Gomm, J. B., *Int. J. Eng. Sci. Technol.* **2**(10), 56–66 (2010).
Shan, Yuyao and Choe, Song-Yul, *J. Power Sour.* **145**(1), 30–39 (2005).
Siegel, J. B., McKay, D. A. and Stefanopoulou, A. G., *in* 2008 American Control Conference, Westin Seattle Hotel, Seattle, Washington, USA, pp. 2573–2578. (2008).
Sun, J. and Kolmanovsky, I. V., *IEEE Trans. Control Syst. Technol.* **13**(6), 911–920 (2005).
Sun, Pengtao and Zhou, Su, *in* Proceedings of ASME 2009 7th International Fuel Cell Science, Engineering and Technology Conference, pp. 299–313. (2009).
Sun, Pengtao and Zhou, Su, *J. Fuel Cell Sci. Technol.* **8**(1), 011010.1–011010.24 (2011).
Sun, Pengtao, Zhou, Su and Liang, Guoping, *Commun Comput. Phys. (CiCP)* **11**(1), 65–98 (2012).
Talj, R. J., Hissel, D. Ortega, R., et al. *IEEE Trans. Ind. Electron.* **57**(6), 1906–1913 (2010).
Talj, R. J., Ortega, R. and Hilairet, M., *Int. J. Control* **82**(9), 1706–1719 (2009).
Tekin, M., Hissel, D., Pera, M. C. and Jauffmann, J. M., *J. Power Sour.* **156,** 57–63 (2005).
Vahidi, A., Kolmanovsky, I. and Stefanopoulou, A., *IEEE Trans. Control Syst. Technol.* **15**(1), 86–98 (2007).
Vahidi, A., et al. *IEEE Trans. Control Syst. Technol.* **14**(6), 1047–1057 (2006).
Wang, Chaoyang, *J. Electrochem. Soc.* **104,** 4727–4766 (2004).
Wang, R. M., Cao, G. Y. and Zhu, X. J., *J. Renew. Energy Resour.* **25,** 70–72 (2007).
Wang, Yun and Wang, Chaoyang, *Electrochim. Acta* **50,** 1307–1315 (2005).
Webb, D. and Moller-Holst, S., Measuring individual cell voltages in fuel cell stacks. *J. Power Sour.* **103,** 54–60 (2001).
Wendeker, M. Malek, A., et al. *SAE Paper* (2007) 2007-01-2012.
Wu, K., Ma, T. C., Zhou, Y., Shen, X. Y. and Zhou, S., *J. Qingdao Univ.* **23,** 20–25 (2008).
Xiao, Y., Ming, P. W. Hou, M., et al. *J. Power Sour.* **188,** 163–169 (2009).
Yang, W. C., Bates, B., Fletcher, N. and Pow, R., *SAE Paper* **98C054** (1998).
Yi, B. L., ''Fell Cell—Theory, Technology and Applications''. Chemical Industry Press, Beijing (2003).

Ying, Wang and Minggao, Ouyang, *J. Power Sour*. **164**(2), 721–729 (2007).
Zhai, Shuang, Chen, Fengxiang and Zhou, Su, *in* Proceeding of 2010 WASE International Conference on Information Engineering (ICIE 2010), Vol. 3,Beidaihe, China, 16–17 August, 2010, pp. 332–335. (2010a).
Zhai, Shuang, Sun, Pengtao, Chen, Fengxiang, Zhang, Chuansheng and Zhou, Su, *in* Proceedings of ASME 2010 8th International Fuel Cell Science, Engineering and Technology Conference, June 14-16, Brooklyn, New York, USA, FuelCell2010-33059, pp. 481–488. (2010b).
Zhai, Shuang, Sun, Pengtao, Chen, Fengxiang, Zhang, Chuancheng and Zhou, Su, *Int. J. Hydrogen Energy* **35,** 8772–8782 (2010c).
Zhang, Yangjun, Minggao, Ouyang, Qingchun, Lu, Jianxi, Luo and Xihao, Li, *Appl. Ther. Eng.* **24**(4), 501–513 (2004).
Zhou, Su., *J. Qingdao Univ.* **19**(1), 78–86 (2004).
Zhou, Su., Zhai, Shuang, Sun, Pengtao, Chen, Fengxiang and Sundmacher, Kai, *J. Fuel Cell Sci. Technol.* **9**(1), 011014.1–011014.8 (2012).
Zhou, Su., Zhang, Chuansheng and Chen, Fengxiang, *J. Syst. Simul.* **23**(7), 1469–1476 (2011b).
Zou, Zhiyu, Zhou, Su and Chen, Fengxiang, *J. Qingdao Univ. Eng. Technol. Ed.* **24**(4), 30–37 (2009).